

TECHNISCHE UNIVERSITÄT MÜNCHEN

Physik-Department E62 – Dense and Strange Hadronic Matter

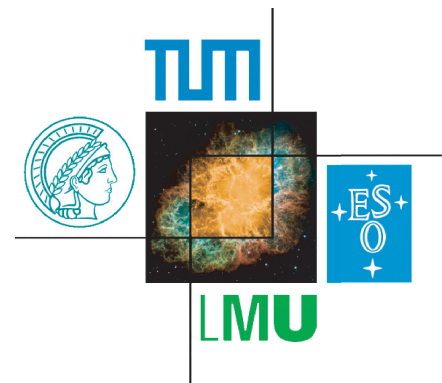
Excellence Cluster – Origin of the Universe

**A Silicon Vertex Tracker for the ${}^8\text{He}(p,p\alpha){}^4\text{n}$
Reaction at SAMURAI**

— MASTER THESIS —

Florian Xaver Dufter

October 12, 2018



First reviewer: Prof. Dr. Laura Fabbietti
Second reviewer: Prof. Dr. Bastian Märkisch
Scientific supervisor: Dr. Roman Gernhäuser

Erklärung

Ich versichere hiermit, dass ich die von mir eingereichte Abschlussarbeit selbstständig verfasst und keine anderen als die angegebenen Quellen und Hilfsmittel benutzt habe.

Ort, Datum, Unterschrift

Abstract

The inner compound of neutron stars is still a fascinating mystery today. Precise measurements of the mass of the neutron star PSR J1614-2230 using the Shapiro-delay revealed the existence of neutron-stars with masses of up to $2.0 M_{\odot}$. To allow very heavy neutron star masses at radii between 11-14 km, a stiff equation-of-state is mandatory. However, at high densities, the creation of particles with strangeness is energetically favorable and introduces a new degree of freedom. This mechanism softens the rigidity in the equation-of-state and contradicts the existence of heavy neutron stars. Three- and four-body forces among neutrons in dense environments can introduce a hardening on the E.o.S. to allow for neutron-star masses up to $2.0 M_{\odot}$ at moderate radii. Chargeless nuclei consisting of neutrons are believed to play an important role in high-density environments such as the inner core of neutron stars. The tetra-neutron (${}^4\text{n}$) is a hypothetical bound state of four neutrons, which is believed to exist in these harsh environments. While the ground state is believed to be unbound due to the antisymmetry of the wave function, theoretical models predict bound resonances. In 2016 Kisamori et al. observed a resonant ${}^4\text{n}$ state close to threshold in the missing-mass spectrum of the double-charge-exchange reaction ${}^4\text{He}({}^8\text{He}, {}^8\text{Be}){}^4\text{n}$ at 186 AMeV with a significance of 4.9σ . The SAMURAI19 experiment at the RIBF at the RIKEN Nishina Center in Japan aims at producing and investigating the ${}^4\text{n}$ system in the quasi-free scattering reaction ${}^8\text{He}(\text{p}, \text{p}\alpha){}^4\text{n}$ in inverse kinematics at 156 AMeV using the missing-mass spectroscopy. Additionally, the produced ${}^4\text{n}$, and its final state interaction products are registered by a highly efficient detection system for chargeless particles. To achieve a missing-mass resolution of 1.6 MeV (FWHM) on the measurement instrument, a silicon vertex tracker has been developed within the framework of this thesis. The tracker consists of six single-sided 100 μm thick silicon strip detectors with an area of $5 \times 8 \text{ cm}^2$ and a granularity of 100 μm for vertex reconstruction in three dimensions. The layers are organized in three distinct modules for readout in X and Y and are placed at distances of 12 cm in a vacuum chamber with a direct connection to the liquid-hydrogen target (MINOS). The distance between the tracker and the target has been minimized to optimize the spatial and angular resolution. A GEANT4 simulation of the tracker set constraints of the vertex reconstruction in beam direction of $\sigma_z = 1 \text{ mm}$ to resolve the ${}^4\text{n}$ resonance. The silicon tracker has been used at the SAMURAI19 experiment in Japan. A thorough calibration of the tracker as well as data analysis has been performed. After applying clustering and track-finding algorithms, the vertices of charged particles have been reconstructed. The angular resolution is determined to 0.84 mrad. Empty target runs were used to determine the distance-dependent spatial resolution in beam-direction of the tracker, which showed to range from $\sigma_z = 0.68 \text{ mm}$ in the front of the target to around 1.73 mm in the back for all opening-angles. The energy losses of particles originating from vertices in the target have been investigated for patterns. Four accumulation regions hint at reactions where ejected particles obey a certain energy-loss scheme. Angular distributions have been investigated. Events with one particle having an energy loss of 100 keV in combination with another particle losing energy of 300-450 keV, an excess of events with an opening angle of 3° is visible. The out-of-plane angle between the beam and the plane, which is spanned by the two charged particles, has been investigated for possible three-body-productions. Further investigation by combining the data with information obtained by other subdetectors is ongoing.

Zusammenfassung

Der Aufbau von Neutronensternen ist noch immer nicht vollständig geklärt. Die Bestimmung der Masse des Neutronensterns PSR J1614-2230 mit Hilfe des sog. "Shapiro-delays" offenbarte die Existenz von Neutronensternen mit Massen schwerer als $2.0 M_{\odot}$. Die sog. "Equation-of-state" gibt die Beziehung zwischen Druck und Energie für dichte Materie an und bedarf eines steifen Verhaltens für die Existenz von schweren Neutronensternmassen bei kleinen Radien von 11-14 km. In dicht gepackter Materie ist die Umwandlung von Neutronen in Teilchen mit Strangeness energetisch günstig. Dieser neue Freiheitsgrad schwächt die Steigung in der "Equation-of-State" ab und schließt somit die Existenz von schweren Neutronensternen aus. Hypothetische Drei- und Vierkörperwechselwirkung zwischen Neutronen in dichten Umgebungen könnten jedoch zu einem steiferen Verhalten der EoS beitragen und somit wieder die Existenz von schweren Neutronensternen bei moderaten Radien erlauben. Ungeladene Kerne bestehend aus Neutronen spielen eine wichtige Rolle in dichten Umgebungen wie dem Inneren von Neutronensternen. Das Tetra neutron (${}^4\text{n}$) ist ein hypothetischer gebundener Zustand aus vier Neutronen welcher in diesen grenzwertigen Bedingungen existieren könnte. Theoretiker sind sich einig, dass der Grundzustand aufgrund der Antisymmetrisierung der Wellenfunktion nicht gebunden ist. Für höher angeregte Zustände ist dies jedoch nicht klar und theoretische Modelle sagen gebundene Zustände voraus. Kisamori et al. beobachtete im Jahre 2016 eine ${}^4\text{n}$ Resonanz nahe an der energetischen Schwelle im Missing-mass Spektrum der Reaktion ${}^4\text{He}({}^8\text{He}, {}^8\text{Be}){}^4\text{n}$ bei Energien von 186 AMeV mit einer Signifikanz von 4.9σ . Das SAMURAI19 Experiment am RIBF des RIKEN Nishina Centers in Japan verfolgt die Untersuchung von ${}^4\text{n}$ -Systemen in der quasi-freien Streureaktion ${}^8\text{He}(p, p\alpha){}^4\text{n}$ in inverser Kinematik bei Energien von 156 AMeV mit der Missing-mass Spektroskopie. Zusätzlich wird das erzeugte ${}^4\text{n}$ und etwaige Zerfallsprodukte mit hocheffizienten Neutronendetektoren untersucht. Im Rahmen dieser Arbeit wurde ein Siliziumtracker entworfen um eine Energieauflösung von 1.6 MeV (FWHM) zu erreichen. Er besteht aus sechs einseitigen $100\ \mu\text{m}$ dicken Siliziumstreifendetektoren mit einer effektiven Fläche von $5 \times 8\ \text{cm}^2$ und einer Granularität von $100\ \mu\text{m}$ für die Vertexrekonstruktion in X, Y und Z. Die Detektoren sind in drei Modulen mit je einem X- und einem Y- Detektor eingefasst und in Abständen von 12 cm in einer Vakuumkammer platziert. Der Abstand zwischen Tracker und MINOS wurde minimiert für eine optimale räumliche Auflösung. Eine GEANT4 Simulation setzt die Grenze für die Auflösung in Strahlrichtung zu 1 mm um die Resonanz zu beobachten. Nach Kalibration, Cluster- und Tracksuche wurden die Vertices der geladenen Teilchen rekonstruiert. Ereignisse mit leerem Target wurden für die Bestimmung der räumlichen Auflösung in Strahlrichtung benutzt. Die Winkelauflösung beträgt $0.84\ \text{mrad}$. Die räumliche Auflösung in Strahlrichtung, σ_z wurde für Anfang und Ende des Targets bestimmt zu jeweils $0.68\ \text{mm}$ und $1.73\ \text{mm}$ für alle Öffnungswinkel. Der Energieverlust von produzierten Teilchen aus dem Target wurde untersucht. Vier Bereiche mit erhöhter Statistik geben Hinweise auf unterschiedliche Reaktionen. Für Kombinationen von einem Teilchen mit einem Energieverlust von ca. $100\ \text{keV}$ mit einem Teilchen mit $E_{\text{loss}} = 300\text{-}450\ \text{keV}$ zeigt sich eine statistische Häufung bei einem Öffnungswinkel von ca. 3° . Der relative Winkel zwischen dem Strahlteilchen und der von beiden Produktteilchen aufgespannten Ebene wurde auf mögliche Dreiteilchenproduktion untersucht. Die Datenanalyse in Kombination mit anderen Detektoren des Experiments wird durchgeführt um weitere Rückschlüsse ziehen zu können.

Contents

1	Introduction	1
1.1	Production reaction	3
1.2	Missing-mass spectroscopy	5
2	Experiment	7
2.1	Setup configuration	8
2.2	MINOS target	10
3	Concept of the silicon tracker	13
3.1	Resolution constraints	13
3.2	Tracking concept	16
3.2.1	Silicon wafer	17
3.2.2	Detector module design	18
3.3	Tracker chamber	21
3.4	Target connection	23
4	Digital Readout	25
4.1	Baseline restoration and zero suppression	25
4.2	Pulse shape analysis	27
5	Analysis and discussion	29
5.1	Energy calibration	30
5.1.1	Amplifier gain correction	30
5.1.2	Linear calibration	30
5.2	Clustering	31
5.3	Track selection	32
5.4	Angular resolution	35
5.5	Vertex reconstruction	36
5.6	Target reconstruction	38
5.6.1	Empty target reconstruction	38
5.6.2	Absolute position and resolution	40
5.6.3	Dominating contributions	41
5.6.4	Full target reconstruction	42
5.7	Detector efficiency	45
5.8	Event characterization	46
5.9	Angular pattern	47
5.9.1	Relative angles to the beam axis	47

5.9.2	Opening angle distribution	50
5.10	Out-of-plane transfer	53
6	Summary and outlook	57
7	Appendix	59
7.1	Y layer	59
7.2	APV gain correction	61
7.3	Incompletely filled target	64
7.4	Helium-6	65
7.5	Concept drawings	68
	Bibliography	75
	Acknowledgement	77

1 Introduction

In 2010 Demorest et al. measured the mass of the pulsar PSR J1614-2230 with unprecedented precision [1]. The mass of this neutron star has been determined to $1.97 \pm 0.04 M_{\odot}$ with a radius of 11 – 14 km. To achieve this density, the equation-of-state must exhibit a stiff behavior. Different approaches try to model the mass-to-radius relation to shine light on the composition of particles in the neutron star (see Fig. 1.1).

The PNM (green line) assumes a composition of pure neutron matter. This model contradicts the so-called Hyperon puzzle, which states that for high densities, the onset of hyperons is energetically favorable [3].

Hyperons are baryons containing one or more strange quarks. Hyperons can be formed as soon as the chemical potential of neutrons, which is a function of the density, is sufficiently high, e.g., $\mu_{\Lambda} \leq \mu_n$. Then the most-energetic neutrons can convert into a Λ . As a result,

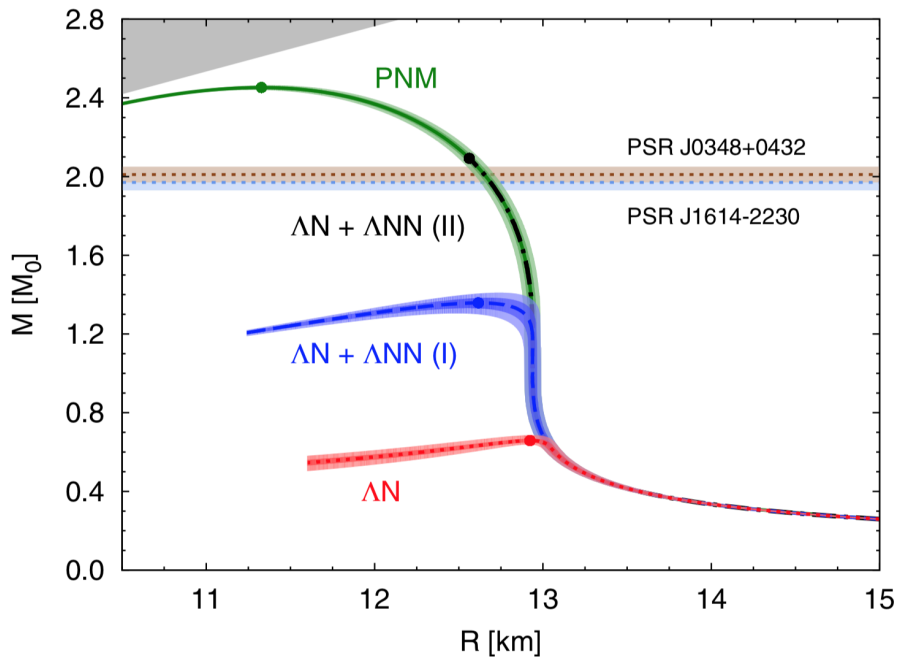


Figure 1.1: Mass-to-radius models for neutron stars which assume pure neutron matter (green line), hyperon-nucleon interaction (red line) or hyperon-nucleon and hyperon-nucleon-nucleon three body forces (blue and black line). The measured mass of PSR J1614-2230 is inserted. Figure taken from [2].

hyperons form in the neutron star and effectively soften the equation-of-state so that large masses are not within reach anymore.

Introducing a hypothetical three-body force is indicated as the blue and black line, where the latter can describe the mass of PSR J1614-2230 by introducing repulsive forces. Three and four-body forces could in principle disentangle this puzzle [4, 5]. However, until now, no interactions of this kind have been observed. To test the existence of three- and four-body forces, multi-neutron systems seem to be a promising probe. Multineutron systems are believed to play an important role in dense environments such as neutron stars [1, 6], where densities up to several times of ρ_0 are achieved.

While neutron-neutron interaction is repulsive due to the antisymmetrization of the wave function, theoretical models predict shallow bound resonance systems of four neutrons slightly above 0 MeV with the requirement of an attractive interaction [7]. Ab-initio calculations predict a resonance state of four neutrons if there is a strong 4-body interaction among the nucleons [8].

By observing the final state of ^4n systems, the interaction among the neutrons can be investigated. Therefore, the energy in the multi-neutron system, as well as the decay pattern, has to be determined. Several attempts have been made to produce systems of four neutrons in the past at low excitation energies:

Marqués et al. [9, 10] presented a new method for production and detection of multi-neutron clusters based on the breakup of beams of neutron-rich nuclei and the detection of multi-neutron clusters in liquid scintillator modules. In the ^{14}Be beam, six events have been identified with characteristics, which are in agreement with the production of multi-neutron clusters in the breakup-reaction $^{14}\text{Be} \rightarrow ^{10}\text{Be} + ^4\text{n}$.

A resonant 4n state was observed by Kisamori et al. in 2016 [11] using the missing-mass method. In the double-charged exchange reaction, $^4\text{He}(^8\text{He}, ^8\text{Be})^4\text{n}$ at 186 A MeV few events were classified with a significance of 4.9σ . In the corresponding missing-mass spectrum (see Fig. 1.2) the background is depicted as the blue line. The combination of background and continuum is indicated as a red line. A broad direct decay structure for energies higher than 5 MeV is expected due to the increasing phase space of the unbound system. Unclear remains the low-energy peak at 0 MeV, which is interpreted as a possible resonant or bound state of the tetra-neutron system.

The small number of significant events motivate for a new experiment with higher statistics, better energy resolution, and an even more clean production pattern. An international collaboration (SAMURAI19 [12]) proposed to investigate the 4n system in the quasi-free scattering reaction $^8\text{He}(p, p\alpha)^4\text{n}$ in inverse kinematics using the missing mass spectroscopy and the simultaneous measurement of the emitted neutrons. This kind of measurement using complete kinematics is unique as it allows to determine the excitation energy in the charged particle branch as well as in the decay neutrons redundantly.

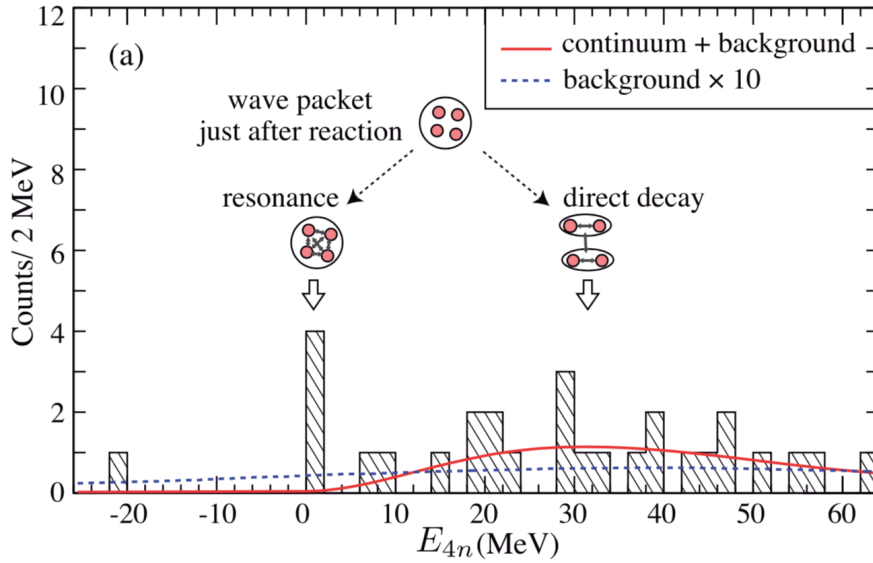


Figure 1.2: Missing-mass spectrum for the ${}^4\text{n}$ measured by Kisamori et. al. The continuum and background are indicated by the red line. The peak at $E_{4n} \sim 0$ MeV is interpreted as a short-living resonance of four neutrons. Figure taken from [11].

1.1 Production reaction

Previous experiments could identify typically few events, which were linked to the production of a tetra-neutron. The lack of statistics, the limited energy resolution and the lack of a direct measurement circumvent to draw further conclusions on the properties of the tetra-neutron resonance.

In a new experiment, the number of significant events is increased by using a higher beam rate as well as a thicker target. Therefore, a liquid-hydrogen target with a length of 5 cm is employed. The energy resolution is improved by using the SAMURAI magnetic spectrometer, which has a momentum resolution of $dp/p = 0.7 \times 10^{-3}$ [13]. To suppress the occurrence of additional reactions and gain further insight on the nature of the ${}^4\text{n}$ the reaction ${}^4\text{He}({}^8\text{He}, p){}^4\text{n}$ at 156 A MeV is used. The final state neutrons of the tetra-neutron resonance are directly measured with the high acceptance neutron detectors NeuLAND and NEBULA.

As schematically drawn in Fig. 1.3, the ${}^4\text{n}$ is produced in a quasi-free knockout reaction. The ${}^8\text{He}$ beam particle is centrally colliding with a proton in the liquid hydrogen target (MINOS) at a lab energy of 156 A MeV, transferring a high momentum onto the proton. This reaction ejects the α -particle core with $E_\alpha = 55$ A MeV and the knocked-out proton with a rather high lab energy of $E_p = 400$ MeV at an average opening angle of $\sim 4^\circ$. The four remaining neutrons are then emitted in beam direction. Due to the high momentum-transfer, the ${}^4\text{n}$ is not affected by the produced charged particles. When observing this reaction in the center-of-mass frame, the charged particles are scattered at large center-of-mass angles, leaving the ${}^4\text{n}$ at rest, which allows observing the final state interaction of the ${}^4\text{n}$.

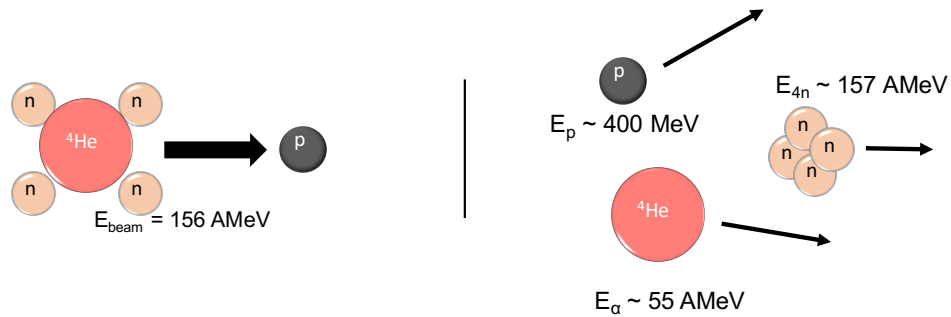


Figure 1.3: Sketch of the 4n knockout production before and after the $^8\text{He}(p, p\alpha)^4n$ reaction. The inner α -core as well as the proton are separated from the four residual neutrons. The expected reaction pattern consists of a fast proton as well as a slow α -particle.

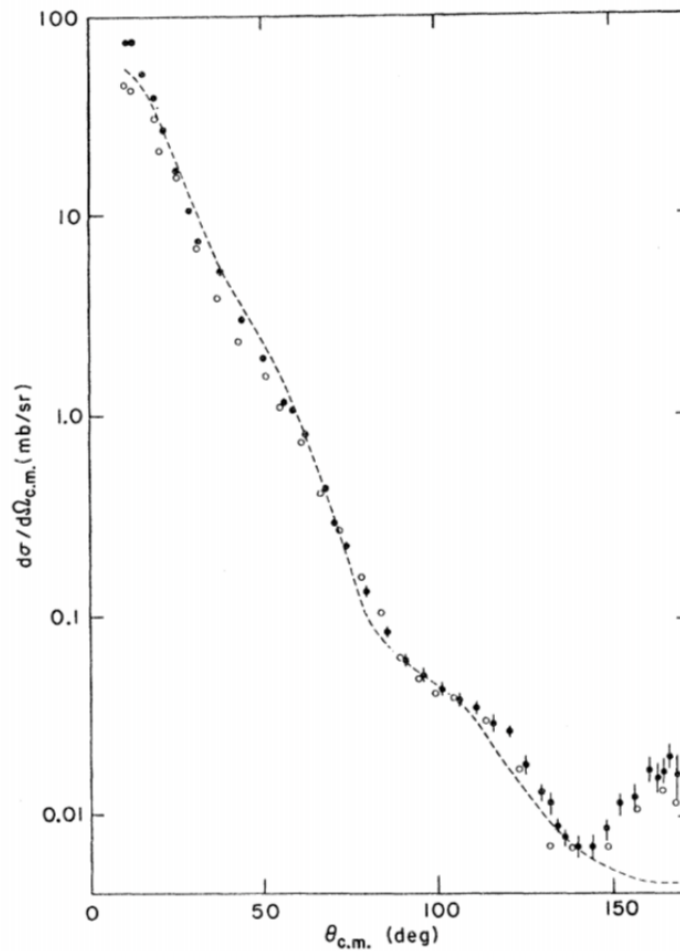


Figure 1.4: Measured elastic differential cross-section for α -proton scattering at 156 A MeV (black dots) and 147 A MeV (white circles) in the center-of-mass frame. A fit given by the optical potential is indicated as the dashed line. Inelastic effects appear at large $\theta_{c.m.}$. Figure taken from [14].

The energy of the ^8He -beam is chosen to be 156 AMeV, so that the particles are quickly separated due to the high momentum transfer between the α -particle and the proton. At this energy, the reaction products move fast enough through the detector without being significantly rescattered while also having an energy loss, which allows them to be tracked. In Fig. 1.4 the elastic cross-section for proton- α scattering as well as the measured cross-section is depicted. The anticipated reaction has an opening angle of $\theta_{c.m.}$ of $\sim 180^\circ$ in the center-of-mass frame. At $\theta_{c.m.}$ larger than $\sim 150^\circ$, the measured reaction cross-section rises, since inelastic effects come into play. At this point, the energy transfer is large enough to separate the α -particle from the beam particle.

This concept sets additional constraints on the energy resolution and the type of the used detectors. The thick target imposes effects like rescattering and energy loss on the charged particles, which add up to a deteriorated energy resolution. Especially the point of production in the target has to be determined to calculate the expected energy loss. The two charged particles have very different energies, which forces to use detectors with a high acceptance in a broad energy range. Finally, the efficiency for detecting several neutrons in coincidence and separating their signals is rather low. To compensate for this two neutron detectors are used.

1.2 Missing-mass spectroscopy

Missing-mass spectroscopy is based on the concept of energy and momentum conservation. It is assumed that the overall energy in the system consisting of particle masses, binding energies, and kinetic energies is conserved and that these can be converted into each other.

Conceptual, the missing-mass is determined by subtracting the total energies of all outgoing particles from the energies of the incident particles. A difference in energy is the available energy for a particle, which was not detected. The scattering mechanism in terms of the conservation of the four-momenta of the particles before and after the reaction is described by:

$$\begin{pmatrix} E_B \\ 0 \\ 0 \\ p_{z,B}c \end{pmatrix} + \begin{pmatrix} m_p c^2 \\ 0 \\ 0 \\ 0 \end{pmatrix} = \begin{pmatrix} E_\alpha \\ p_{x,\alpha}c \\ p_{y,\alpha}c \\ p_{z,\alpha}c \end{pmatrix} + \begin{pmatrix} E_p \\ p_{x,p}c \\ p_{y,p}c \\ p_{z,p}c \end{pmatrix} + \begin{pmatrix} M_{4n}c^2 \\ 0 \\ 0 \\ p_{z,4n}c \end{pmatrix} \quad (1.1)$$

where E_B is the energy of the beam, E_α is the measured energy of the produced alpha-particle, E_p is the energy of the emitted proton and \vec{p}_α and \vec{p}_p are the three vectors of the charged particles. p_{4n} is the momentum of the ^4n and assumed to be parallel to

the momentum of the beam. Using the energy-momentum relationship, the ${}^4\text{n}$ energy in missing-mass spectroscopy is therefore given by the equation:

$$M_{4n} = \sqrt{(E_B + m_p - E_p - E_\alpha)^2 - (\vec{p}_B - \vec{p}_p - \vec{p}_\alpha)^2} \quad (1.2)$$

Since the energy of the particles is defined by the energy-momentum relationship

$$E = \sqrt{p^2 + m^2} \quad (1.3)$$

it is sufficient to determine the particle type (PID) with the mass m_i at rest and the momentum of the particle to reconstruct the total energy E_i . The binding energy of the ${}^4\text{n}$ system is then given by the following equation:

$$B_n = 4 \cdot m_n - M_{4n} \quad (1.4)$$

with M_{4n} being the missing-mass energy and m_n the neutron mass.

2 Experiment

The experiment SAMURAI19 was performed at the SAMURAI (Superconducting Analyzer for Multi-particles from Radioisotope beams) spectrometer at the RIKEN Nishina Center in Japan. The experiment was executed during 6.5 days of beam in May and June 2017. 5.5 days were used for ^8He and proton beams and one day for ^6He on empty and full target each. The particle rate was 2×10^5 pps limited by the rate capability of some elements of the detector setup. The RIBF (Radioactive Isotope Beam Factory) at RIKEN (see Fig. 2.1) consists of several ring cyclotrons, the particle separator BigRIPS and the magnetic spectrometers SAMURAI and SHARAQ. The RIBF can produce exotic high-rate ion beams of unstable nuclei. Currently, the RIBF is the most powerful machine in the world to produce the most exotic beams of unstable nuclei in the light and medium-heavy mass region.

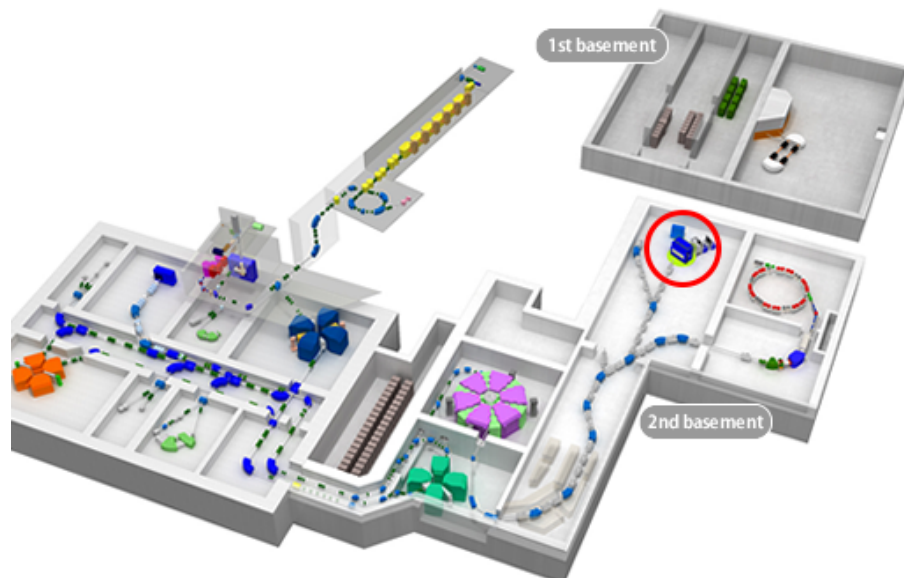


Figure 2.1: Site map of RIBF complex. Indicated are the linear accelerator and the several circular accelerators as well as the bigRIPS particle separator and the magnetic spectrometers SAMURAI and SHARAQ. SAMURAI is indicated by the red circle. Figure taken from [15].

2.1 Setup configuration

Aim of the setup is the exclusive and inclusive measurement of the ${}^4\text{n}$ in the reaction ${}^8\text{He}(p,p\alpha){}^4\text{n}$. The SAMURAI19 setup consists of the high-resolution magnetic spectrometer SAMURAI as well as a variety of smaller detectors as depicted in Fig. 2.3. The inclusive measurement of the ${}^4\text{n}$ puts strict constraints on the energy resolution of the setup and therefore on all sub-detectors, while the exclusive measurement especially challenges the neutron detectors in addition.

First of all, the energy of the charged particles has to be determined with high precision. This indicates a precise simultaneous measurement of the momenta as well as a particle identification. The momenta are determined by measuring the angles and positions of the charged particles before the magnet as well as the positions after the magnet.

The configuration consists of the newly by TUM developed silicon tracker as well as a variety of standard detectors as shown below:

- **SBT (Scintillating Beam Trigger)**: Provides the beam trigger signal when a ${}^8\text{He}$ particle is recognized. Put into a special configuration for this measurement. Starts the time measurement.
- **BDC (Beam Drift Chamber)**: Determines the angle of the beam particle trajectories before the target.
- **MINOS (Magic Numbers Off Stability)**: Cryostat and target bubble filled with liquid hydrogen (LH_2) at a temperature of 20 K.
- **Silicon tracker**: Determines the position of the reaction vertex in the target, the last position of the charged particles before the magnet and the angles of the particle trajectories.
- **SAMURAI-Magnet**: Bends the trajectories of the charged particles with a high precision depending on their charge and momentum.
- **FDC (Forward Drift Chamber)**: Determines the position of the particles after the magnet. Additionally, the particle type is determined by the specific energy loss dE/dx in the gas.
- **HODOscopes**: Large plastic scintillators situated behind the drift chamber. The HODOscopes give the stop signal for the eff. flight-time measurement with high precision and perform particle identification (PID).
- **NeuLAND and NEBULA**: Pair of large acceptance neutron detectors positioned in beam direction after the magnet to perform an exclusive measurement of the energy and decay pattern of uncharged nuclei.

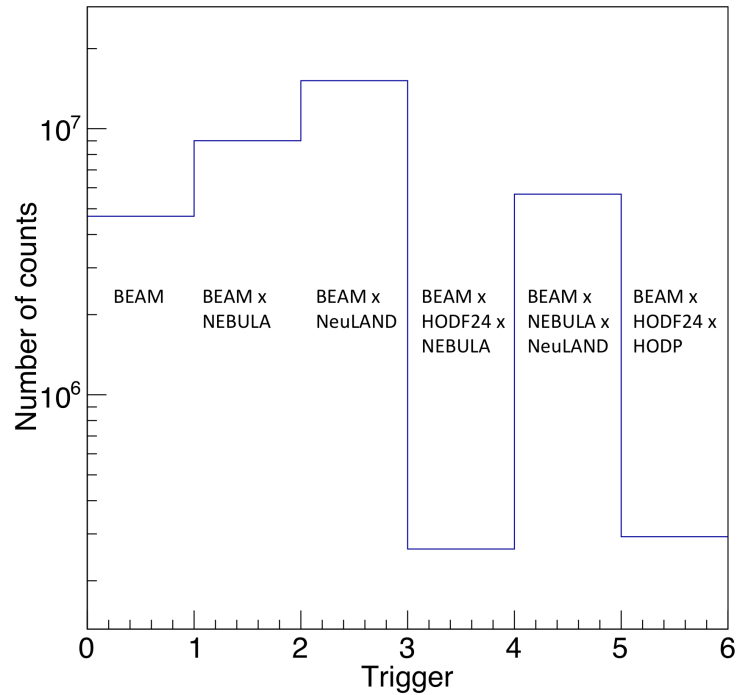


Figure 2.2: Overview of the statistics for forty runs for the different triggers used during the experiment.

Figure 2.2 depicts the statistics for the different triggers recorded in a selection of forty runs. The beam trigger was suppressed. Trigger 4 and 6 are expected to be in particular sensitive to the ${}^4\text{n}$ production since they both require a charged particle in the HODOScopes.

The silicon tracker is a crucial part of the missing-mass spectroscopy. Its task is the precise determination of the particles directions and the position of the reaction vertex inside the target. This approach significantly improves the energy resolution and allows for a precise measurement of the resonance.

For 400 MeV protons and 55 AMeV α -particles, the α -particles are bent about 3.5 times more than the protons. This is indicated in the picture (see Fig. 2.3) as a flip of proton and heavy-ion trajectory. Trajectories of neutrally charged particles like neutrons are not bent by the SAMURAI spectrometer and they move straight to the NeuLAND and NEBULA detectors.

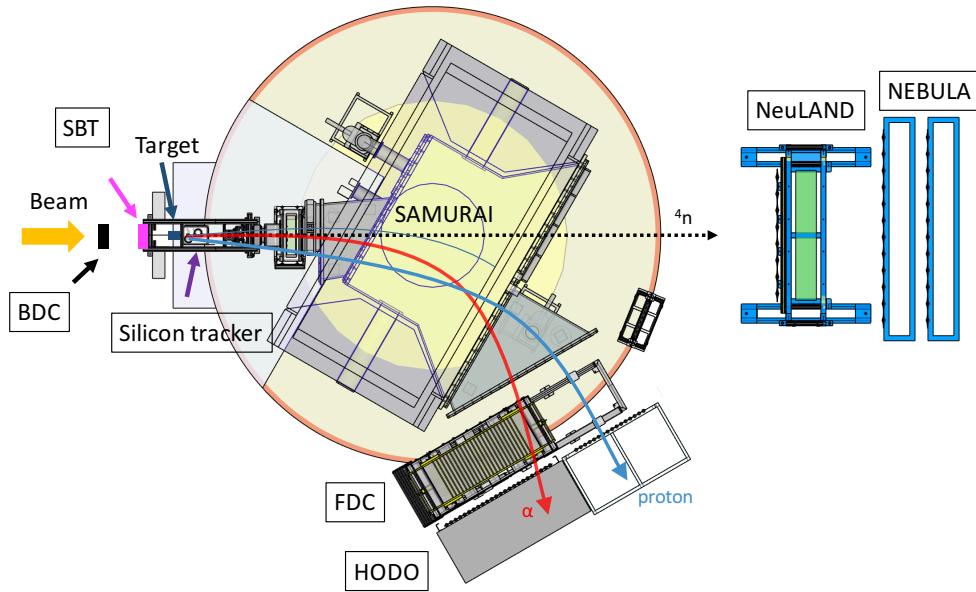


Figure 2.3: Topview of the SAMURAI19 detector setup. The beam is entering the MINOS target from the left side (orange arrow). The target is depicted in blue. The detector setup is triggered by registered events in the SBT, which is indicated in pink. Produced charged particles (red and blue arrow) travel through silicon detector, the SAMURAI spectrometer and are analyzed in the drift chamber and HODOscopes. Produced neutrons (black dotted line) fly straight into the NeuLAND/NEBULA detectors.

2.2 MINOS target

To maximize the number of knock-out reactions while keeping the angular- and energy straggling at a moderate level, a liquid hydrogen (LH_2) target with a density of only 0.07 g cm^{-3} is employed. The MINOS (Magic numbers off stability) target was configured for this experiment with a 5 cm long, 120 μm thick mylar enclosure with a diameter of 4 cm as depicted in Fig. 2.4. It is filled with 20.0 K cold liquid hydrogen from a cryostat located on top [16]. After condensation, the target falls into the target and fills it up rapidly. Cold vapor returns into the target in a closed circuit [17]. MINOS allows for a fast filling and emptying of the target during the runs. The temperature of the liquid hydrogen is kept stable at 20 K throughout the experiment.

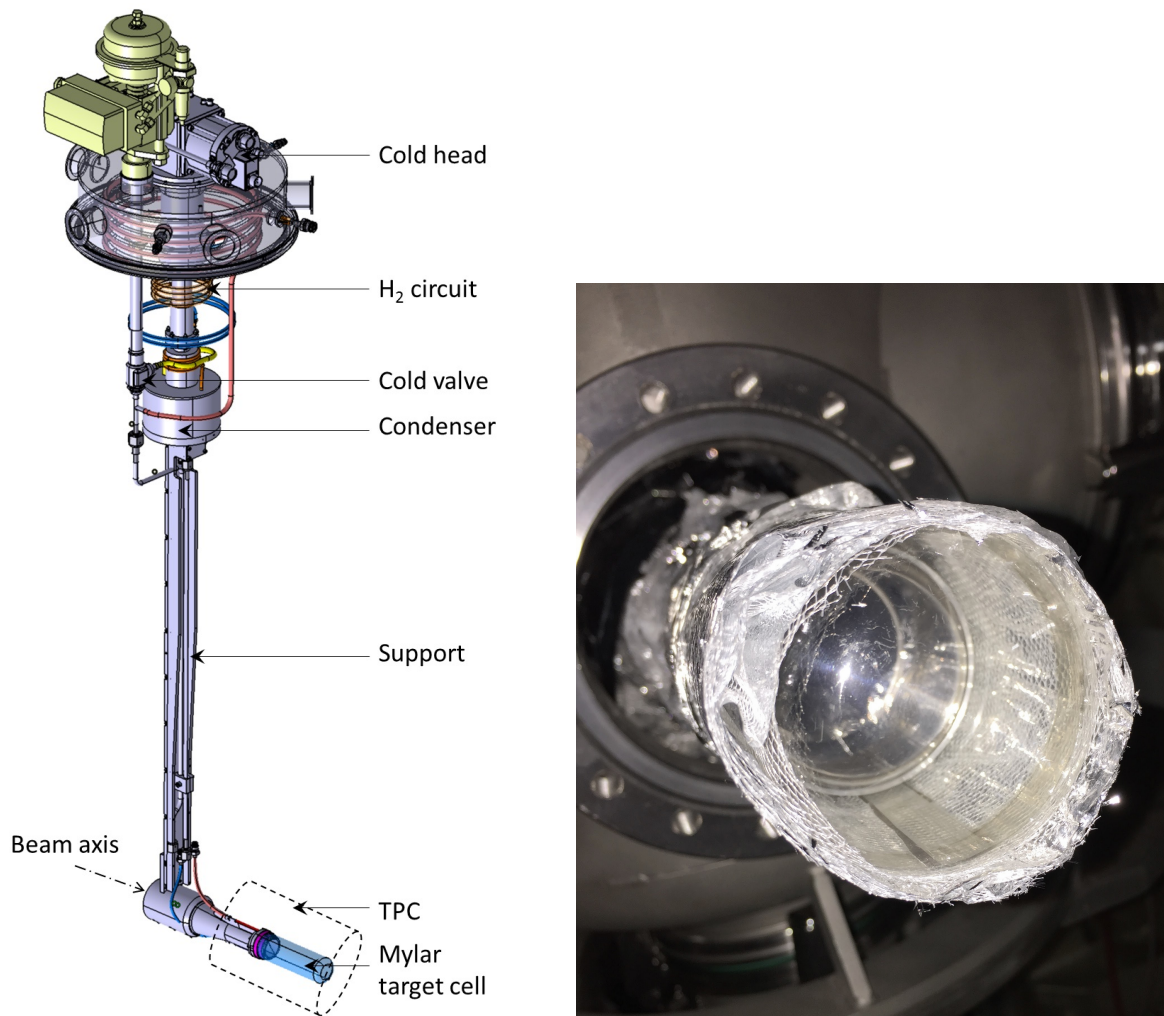


Figure 2.4: Left: Schematic of the MINOS apparatus with cryostat, condenser, support structure and target cell. Figure taken from [17]. Right: Picture of the MINOS target containment. The 120 μm thick enclosure is wrapped with superinsulated foil (aluminum coated thin mylar foil) on the cylindrical sides for enhanced heat isolation.

3 Concept of the silicon tracker

The expected narrow ${}^4\text{n}$ resonance state in the missing mass spectrum sets high constraints on the design of the experiment. To achieve a sufficiently good energy resolution, the tracker has to determine the reaction vertex and the angles and positions of the particles' tracks before the magnet. The lost energy in the target is determined by a vertex reconstruction of the produced charged particles using the ATIMA¹ code to derive the energy loss ΔE from the traveled distances of the ${}^8\text{He}$ and both outgoing charged particles through the material. Apart from the energy loss calculation, the silicon tracker traces the flight directions of the two emitted charged particles to give additional information for the determination of their momenta.

3.1 Resolution constraints

The detector setup as described in chapter 2 is subject to the desired energy resolution in the missing-mass spectroscopy. From a full kinematical simulation of the ${}^8\text{He}(p,p\alpha){}^4\text{n}$ reaction, the influence of different uncertainties is shown in Figure 3.1 for illustration.

The accuracy of the momentum measurement dominates the energy resolution. The contribution to the total energy resolution is 0.53 MeV for a relative momentum resolution of 1.5×10^{-3} for both outgoing charged particles.

An additional contribution altering the invariant mass resolution is the energy loss of particles traversing the target which can be determined by reconstructing the vertex. The resolution of the vertex reconstruction is dominated by the angular scattering of the particles in the material. In tab. 3.1 the scattering of relevant particles in the experiment in 200 μm silicon and 5 cm liquid-hydrogen has been calculated with ATIMA. The low energetic α -particles dominate the energy resolution by the scattering in the target. After introducing the expected straggling in the target and detector, the energy resolution is marked in Figure 3.1.

The resulting energy resolution is given by the quadratic addition of the contributions from momentum and angular measurement:

$$\sigma_E = \sqrt{\sigma_{E,p}^2 + \sigma_{E,\theta}^2} \quad (3.1)$$

¹ <https://web-docs.gsi.de/~aprochaz/webatima/>

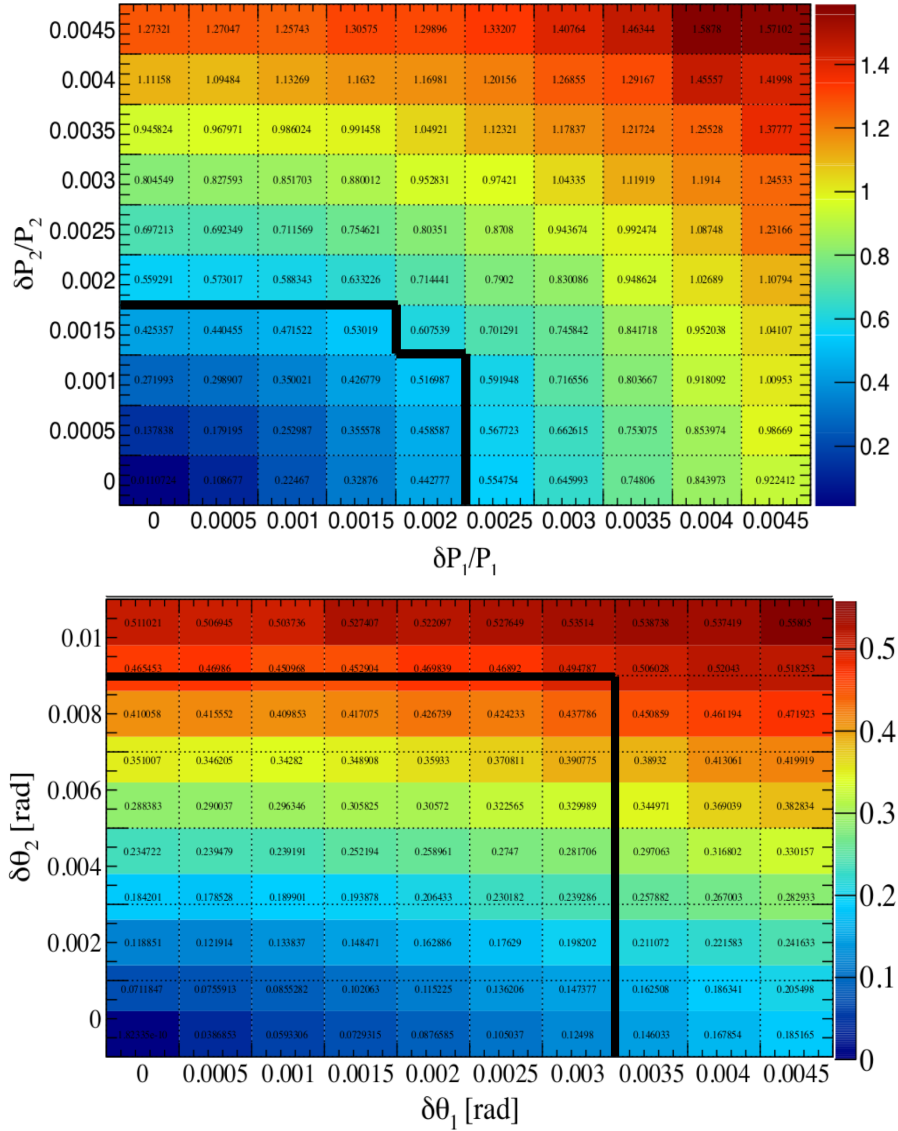


Figure 3.1: Upper: Energy resolution (sigma) of the reconstructed missing-mass in MeV (color code) as a function of the resolution for the momentum measurement of the two charged particles in the outgoing channel. A perfect measurement of the angles is assumed. Lower: Energy resolution (sigma) of the reconstructed missing-mas in MeV (color code) as a function of the resolution for the angular measurement of the two charged particles. A perfect measurement of the momentum is assumed. The allowed parameter regions to achieve an energy resolution of 0.43 MeV (sigma) are indicated. Taken from [12].

Particle	Energy [AMeV]	σ_a in 200 μm Si [mrad]	σ_a in 5 cm LH ₂ [mrad]	E_{loss} in 100 μm Si [keV]	E_{loss} in 5 cm LH ₂ [MeV]
^4He	55	3.6	5.3	987	37.1
^8He	156	0.6	0.9	402	15.6
^1H	400	0.9	1.5	58	2.2
^1H	156	2.3	3.6	101	3.9

Table 3.1: Angular scattering and energy loss of helium and protons in silicon and in the LH₂ target for different energies.

In the proposal, the anticipated total energy resolution for the ^4n system is 0.7 MeV (Sigma), which is sufficient enough to resolve the resonance. As shown in Table 3.1 the multiple scattering in the target dominates the resolution. The big advantage of the vertex reconstruction is that it allows separating the data into different branches. Reactions with vertices in the later part of the target are affected by less straggling of the outgoing charged particles, which results in a better energy resolution. To simulate the expected missing-mass spectrum with this value, a delta function placed at 0 MeV has been folded with the energy resolution of the full setup (see Fig. 3.2). In a second step a more realistic resonance has been modeled with a 3 MeV broad gaussian peak at $E = 3$ MeV. The position resolution becomes worse with increasing distance between the first detector layer and the vertex position due to multiple scattering in the target and detector effects (see Fig. 3.3). Therefore, accounting all events improves the statistics but decreases the missing-mass resolution. By omitting events from vertices in the first half of the target a resulting contribution of 0.43 MeV (see Fig. 3.1) from the angular measurement can be achieved, if necessary.

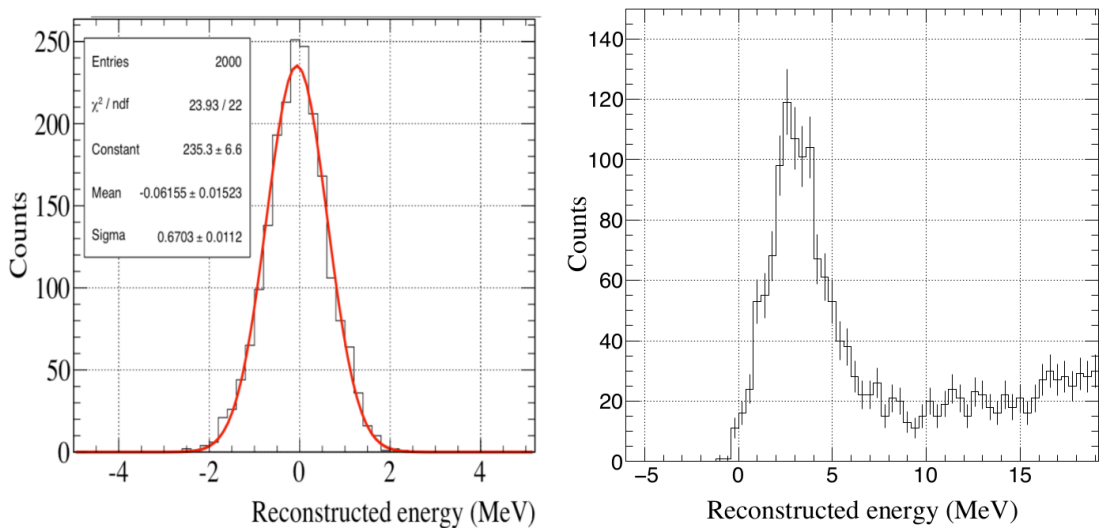


Figure 3.2: Left: Response for the reconstruction of the energy for a delta function situated at 0 MeV. Right: Simulation of the reconstructed energy spectrum with an assumed resonance at 3 MeV with a width of 3 MeV over a non-resonant background. Figure taken from [12].

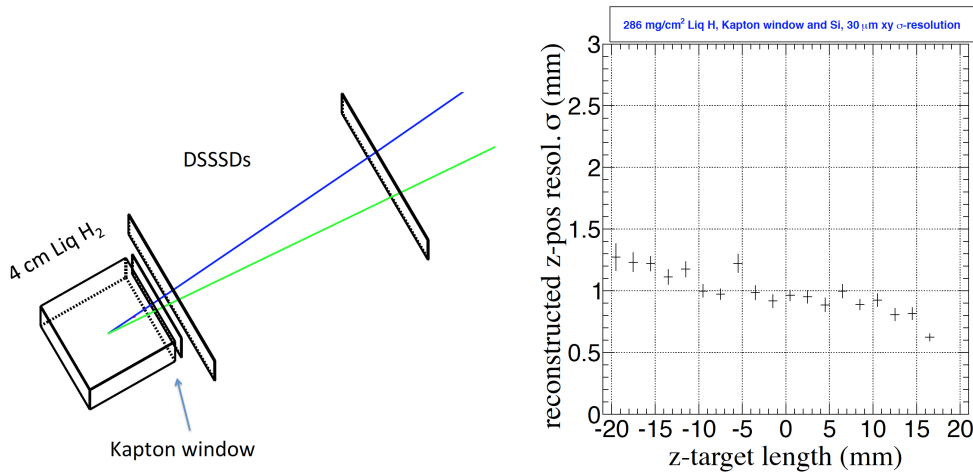


Figure 3.3: Left: Geometry of the target area in the GEANT4 simulation. The vertex is reconstructed from the tracks of the two outgoing charged particles. Right: Resolution dependence on the z-position for the vertex reconstruction in the target. Figure taken from [12].

In total, these additional effects alter the total energy resolution to around 0.81 MeV, which is still good enough to resolve the resonance peak in the spectrum.

3.2 Tracking concept

The particles are traced by their signals in the silicon strips. In Fig. 3.4, the tracking concept of particles emerging from the target is depicted. The beam is entering the target from the left. After the reaction, two charged particles are emitted into the tracker. The silicon layers are schematically drawn as black stripes. The hit-positions of the charged particles are measured as well as their energy deposit.

The vertex reconstruction uncertainty grows with larger distances between the first wafer and the target due to the angular scattering. Therefore, it is necessary to locate the liquid-hydrogen target as close to the detector as possible.

The beam penetrates the target in this Figure from the left. A reaction happens in the target, producing the charged particles, which are then emitted with certain angles with respect to the beam direction. As the charged particles fly through the silicon sections, they deposit energy in the strips which is measured. Besides, there is also multiple scattering so that particles also slightly change their directions in each layer of silicon (see Tab. 3.1).

A reaction vertex is the point of closest approach between two particle tracks. To reconstruct a track at least two hit points are needed to fit a straight line. In principle, the minimum requirements to reconstruct a reaction vertex in three dimensions are two tracks with two points each. A cartoon of this principle with the dimensions of the setup is shown in Fig. 3.5. The particles' directions are then reconstructed with:

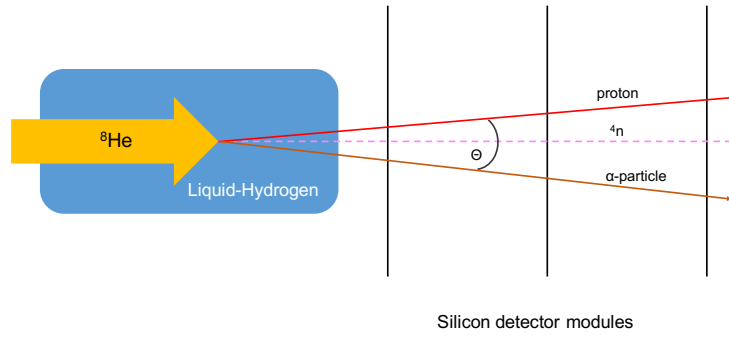


Figure 3.4: Conceptual overview of the vertex tracking. The beam (orange arrow) reacts at a random position along the target (blue area). After the reaction, two charged particles (red and brown track) are emitted into the silicon tracker. The particles leave energy in the strips of the silicon wafers (black lines). The opening angle between the particles as well as the position of the reaction vertex can then be reconstructed. The ${}^4\text{n}$ (pink dotted line) is not depositing energy in the wafers and moves undeflected through the tracker.

$$\begin{pmatrix} S_x \\ S_y \\ S_z \end{pmatrix} = \begin{pmatrix} X_2 \\ Y_2 \\ Z_2 \end{pmatrix} - \begin{pmatrix} X_1 \\ Y_1 \\ Z_1 \end{pmatrix} \quad (3.2)$$

Where S_X , S_Y and S_Z are the slopes in all three dimensions.

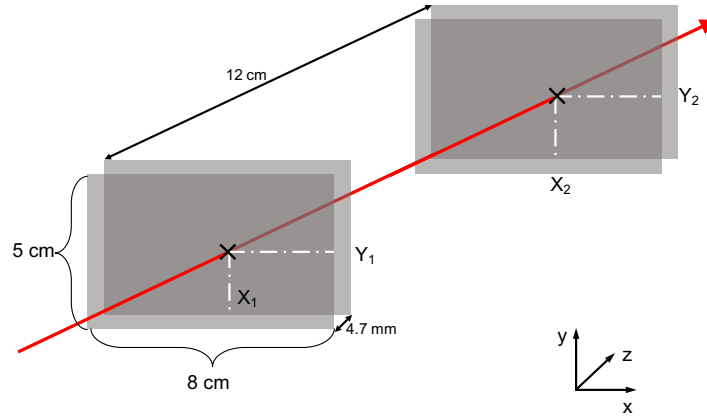


Figure 3.5: Schematic view of the track reconstruction. A particle (in red) penetrates all four wafers and leaves signals in the corresponding channels. The dimensions of the wafers are indicated as well as the distances between the modules and between the detectors.

3.2.1 Silicon wafer

The tracking system has to determine the particle tracks with high angular resolution and the reaction vertex in the target with high precision. This requires a high granularity of the silicon wafers and a thin wafer design to minimize angular straggling.

Single-sided silicon strip wafer with a pitch size of $100\ \mu\text{m}$ and a thickness of $100\ \mu\text{m}$ are employed for this experiment [18]. X- and Y-type wafer are combined in a detection module to provide a hitpoint in both dimensions. Both have the same spatial extension of $5 \times 8\ \text{cm}^2$. The strips of the X-type wafer are oriented vertically, while the Y-type wafer strips are horizontally oriented.

The expected energy loss of the particles in the silicon wafers has been calculated with ATIMA and is depicted in Table 3.1. The wafer thickness is chosen such that it contributes minimally to the angular scattering but also provides enough material for signals of fast protons, which have a low specific energy loss in silicon.

3.2.2 Detector module design

The detector concept is based on single-sided silicon strip detectors with a pitch and thickness of $100\ \mu\text{m}$ only. The wafer cover the whole beam area with a size of $8\ \text{cm} \times 5\ \text{cm}$. A detection module consists of two detection planes, which are stacked together for Y- and X-readout (see Fig. 3.7 and 7.1). The X- and Y-detection planes are mounted on the copper frames with thermal paste applied between the copper and the PCB to improve the heat transfer. The copper frames are attached to the cooling frame, and the fully assembled detection module is then placed inside the chamber. The data is transported via $20\ \text{cm}$ long FFC cables to the feedthroughs, which are located below and next to the modules.

To read out the tiny signals especially of the fast protons a highly integrated system based on the APV25 chip is used [19]. Each APV25 employs 128 channels of a preamplifier and fast shaper as well as a 4068 channels deep analogue range. Every second channel is bonded to the wafer. The unbonded channels are used to calculate and correct the baseline. In Fig.

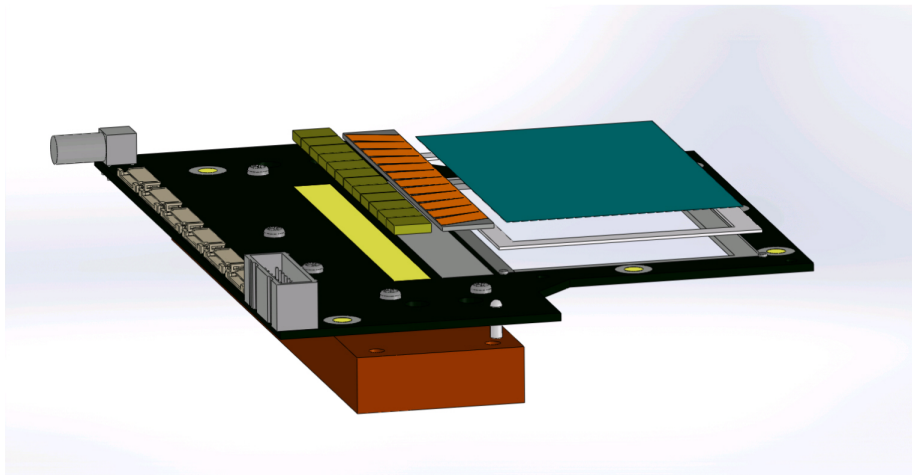


Figure 3.6: Schematic of the X-PCB detector module. The PCB is indicated in black. The wafer (indicated in green) is placed on a ceramic frame. APVs are shown in yellow and the pitch adapter in orange. The PCB is mounted on a copper cooling frame. Adopted from [18].

3.6, a sketch of the X-module is shown. The data is transported to a collecting backplane outside of the vacuum chamber. Closer details are described in Ref. [18].

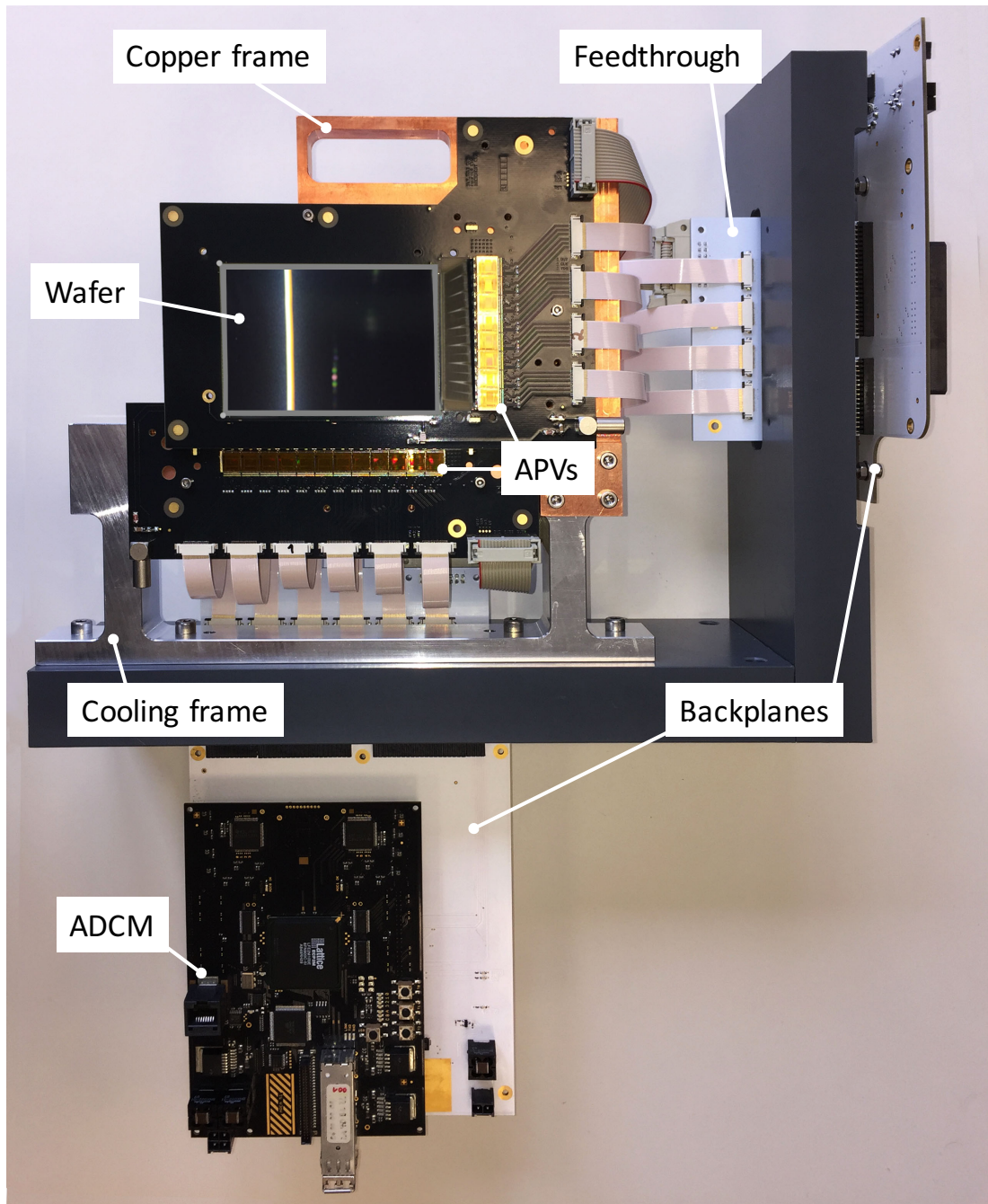


Figure 3.7: Breakout picture of a detector module with marked components. The Y-layer is located on top of the X-layer, the data is read out via FPC cables. The deposited charge in the wafer is read out by the APV25 chips and then transported to the backplane and ADCM. Afterwards, the data is digitized and sent to a TRB3 board.

3.3 Tracker chamber

To achieve stable conditions in the target, the area around MINOS is evacuated. For an optimal vertex reconstruction resolution, the first detector layer has to be placed as close to the target as possible. Therefore, a vacuum-tight solution has been developed. The silicon detectors are contained in a newly designed vacuum chamber, which is connected to the target chamber vacuum tight. The vacuum chamber has dimensions of 49 cm x 36 cm x 27 cm with a wall-thickness of 25 mm (see Fig. 7.10). The chamber has three feedthrough connections on both the bottom and the left side. Removable lids are located on both the top and the right side to support the mounting of the detector modules. The cooling frame is hollow inside, and cooling water is circulating through the metal frame. This construction keeps the APV25 chips at a temperature of 20 °C. The particles are traversing the chamber through the 125 μm thick circular windows in the front and the back.

The vacuum connection to the target is schematically drawn in Fig. 3.9. MINOS is located inside the newly designed flange and the bellow. The bellow is connected vacuum-tight to the MINOS cryostat and the flange on the front side of the tracker chamber. To decouple the detector chamber from possible vibrations coming from the cryostat a vibration damping strain relief was implemented. For electrical isolation, plastic screws and bumpers were used.

On the downstream side of the flange a 2 μm thick aluminized mylar foil was placed to shield the target from emitted heat by the APV25 chips. A safe distance of ~ 6 mm between the first detector layer and the target was manually tuned by the extension of the bellow.

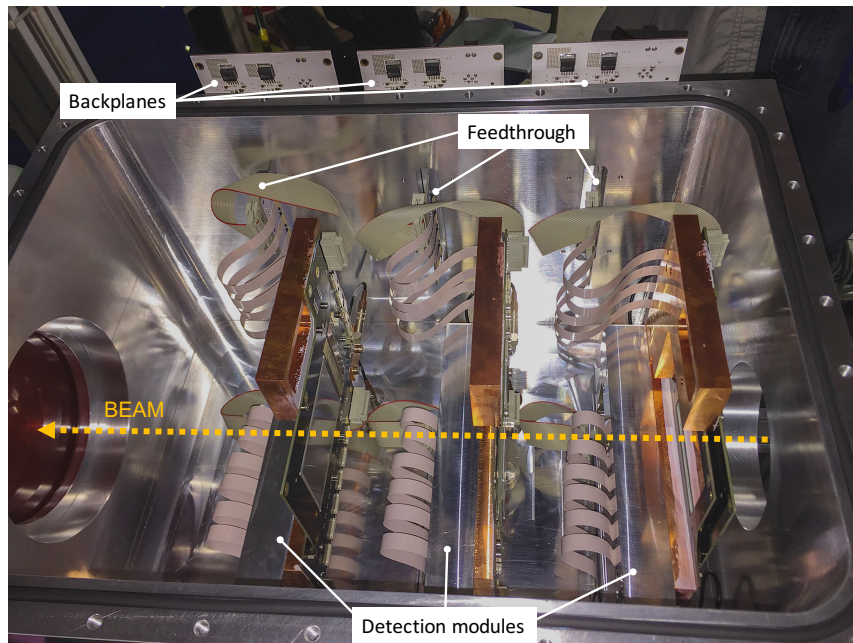


Figure 3.8: Picture of the installed detection modules in the tracker chamber. The beam direction is indicated in orange and the important components are marked.

The whole setup was aligned with the help of laser markers, and absolute positions were determined by using the photogrammetric method. During the experiment, the vacua were stable at a pressure of $\sim 10^{-5}$ to 10^{-6} mbar.

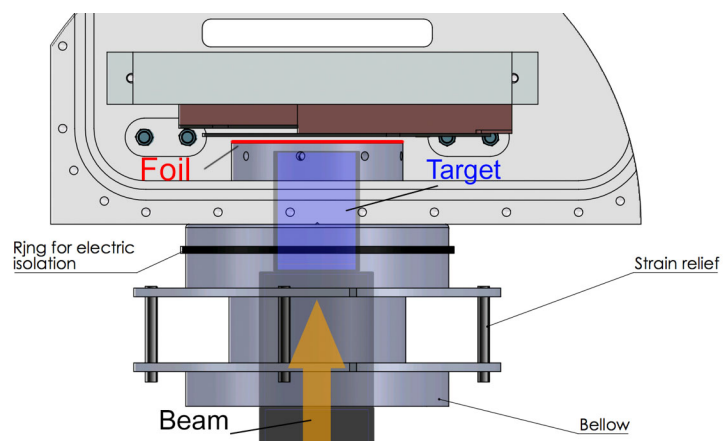


Figure 3.9: Top view of the connection between chamber and target. The position of the target is indicated in blue, the beam direction is shown in orange, and the aluminized mylar foil is depicted in red. To decouple the detector from the target both electrically and mechanically, electric isolation and strain reliefs with bumpers were implemented.

3.4 Target connection

A special connection flange was developed to connect both the MINOS chamber and the chamber of the silicon vertex tracker vacuum-tight, shield MINOS from the emitted heat of the ASIC chips on the silicon tracker by a 2 μm thick aluminum-coated mylar foil, minimize the distance to the first detector layer the material in the particle path. MINOS was located at a distance of only $\sim 5.2\text{ mm}$ to optimize for the angular and the vertex reconstruction resolution of the tracker. The target is kept at a stable temperature of 20 K. The target chamber is evacuated to a pressure of 10^{-7} bar. A picture of the flange is shown in Fig. 3.10.

The flange has a thickness of 27 mm and is perforated with drills to connect both the vacuum from the target chamber and the silicon tracker.

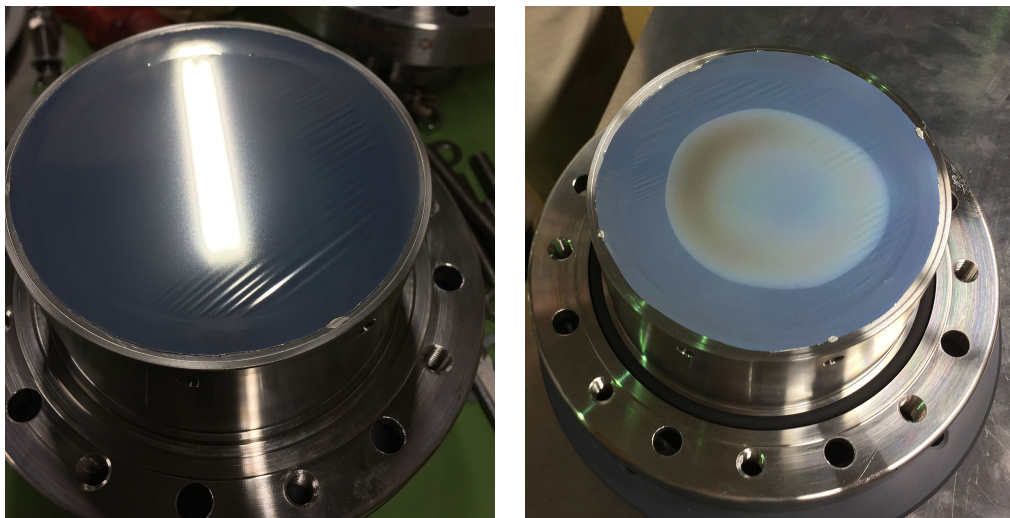


Figure 3.10: Flange with aluminized mylar foil before and after radiation.

4 Digital Readout

The data acquisition system consists of three independent branches, one for the neutron detectors (NeuLAND x NEBULA), for the SAMURAI detectors and a third one for the silicon tracker. These three DAQ branches are connected by the trigger and an independent time-stamping system. Each detector device is read-out event-by-event and marked with a timestamp generated by the master-module LUPU. The slave DAQ of the silicon detectors [20] is embedded in the main, so-called, BABIRL-DAQ which writes the received signals into one merged file in the RIDF data format.

The readout scheme of the silicon detectors is adopted from other experiments with silicon detectors at RIKEN. A TRB3 board receives the trigger signal. Once triggered, the APV25 chips store the corresponding pulse height info of one of the analogue memories and later asynchronously send the signals in the ring-buffer to the digital converters (ADC) on the backplanes. The digitized signals of all APVs are then collected in the TRB3 system, which is responsible for event building and data transmission to the central DAQ.

4.1 Baseline restoration and zero suppression

The grounding in the APV25 chip is affected by incoming charge [18]. Therefore, energy deposition of particles in the strips can modify the baseline of the APV25 signal range. In the case of a hit, the strips in close vicinity are also affected. The information from the unbonded neighbor strips can then be used to apply a baseline restoration for the bonded channel in between.

The noise for every channel is gaussian distributed. The mean is shifted to an ADC value of 0. For the X-type detectors, a noise of $\sigma_x = 15.5$ channels is recorded. Due to the larger strip length of 8 cm, the noise in the Y-type detectors is with $\sigma_y = 18.5$ channels a bit larger (see Fig. 4.2). To reduce the amount of data, a two sigma noise cutoff is directly applied which then equals an ENC of $\sim 2.5\%$.

During an event several strips are found to be above the 2 sigma threshold (see Fig. 4.1).

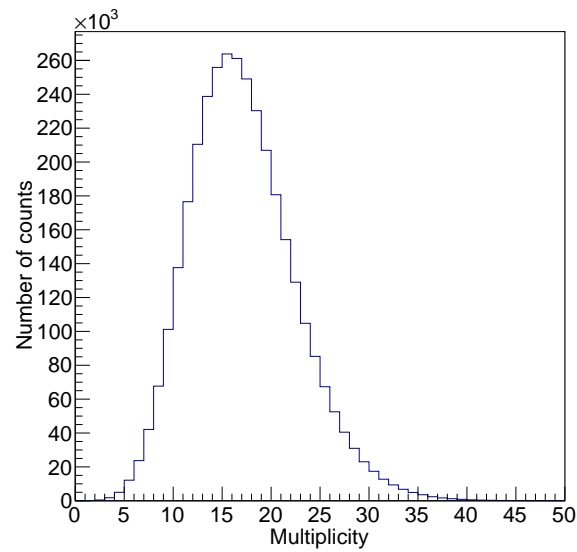


Figure 4.1: Number of strips above the cutoff threshold per event in the first detector layer for an one hour run. Around 17 strips report a signal per event of whom most are noise above threshold.

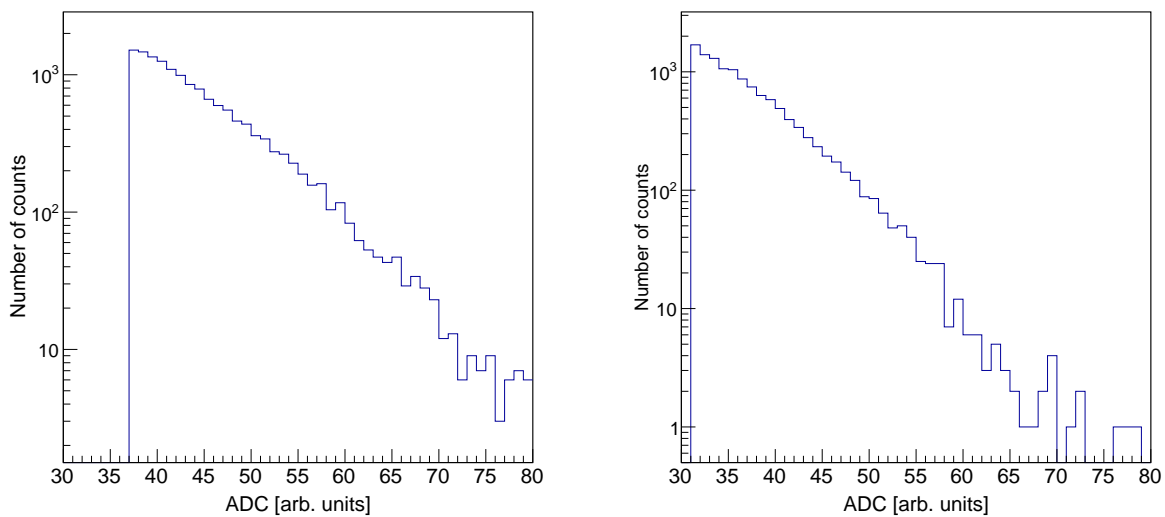


Figure 4.2: Counts in the first strip in the first Y and X detector layer respectively. The exponential noise tail is cut at 37 channels and 31 channels for the Y and X detector type. For this sample, 5×10^5 events were considered.

4.2 Pulse shape analysis

During data acquisition, the energy losses of the particles in the strips are collected. In this time window, an additional particle can also deposit energy in the same strip, which is considered as pile up.

To sort out this contamination, the three sample mode of the APV25 chip was used. The minimum shaping time of the APV25 chip is 75 ns in the single sample mode. The chip can be reprogrammed to take three samples in a single event in a time window of 150 ns. This allows to conduct a pulse shape analysis of the shaper signals to filter events with possible pileup contamination (see Fig. 4.4). The inset shows a typical shaping signal curve depicted in blue. The shaping signal is sampled at three different points in time ($a_1 = \text{ADC}(t = 0)$, $a_2 = \text{ADC}(t = 75 \text{ ns})$ and $a_3 = \text{ADC}(t = 150 \text{ ns})$) at times of 75 ns. The differences between the three samples ($a_3 - a_2$ and $a_2 - a_1$) are then plotted against each other. A valid shaper signal consists of a rising slope followed by a falling slope with the deposited energy being directly proportional to the maximum value. These signals should appear in the quadrant marked as IV, since $a_2 - a_1$ is positive and $a_3 - a_2$ is negative.

Shaping pulses with different waveforms can in general not be used for further analysis since the determination of the maximum is not possible. For example, when beam particles create pile up information during shaping time due to a high beam rate, the value of the samples a_1 or a_3 may be higher than the value of a_2 . Then a linear relation between the deposited energy loss and the signal is not possible anymore. These events appear in the other three quadrants. During full target runs around 8% of all recorded events were identified as pile up and removed from the analysis.

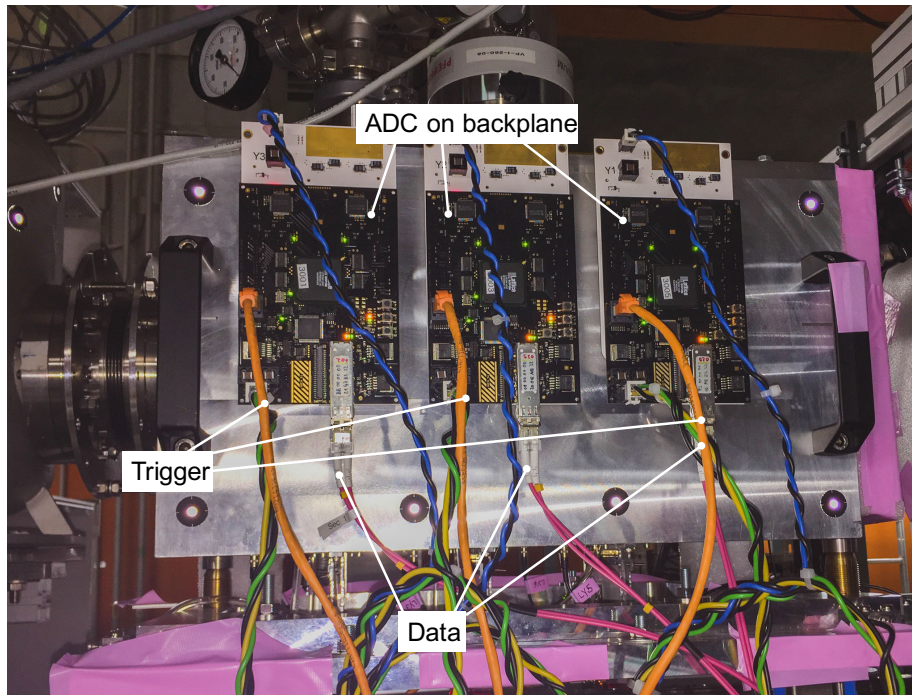


Figure 4.3: Picture of the mounted chamber on the beam line with electronics for data readout. The black ADCM modules are attached to the backplanes. The orange ethernet connection sends the trigger signal. Data is transmitted to the TRB3 board by the glass fiber cables in pink.

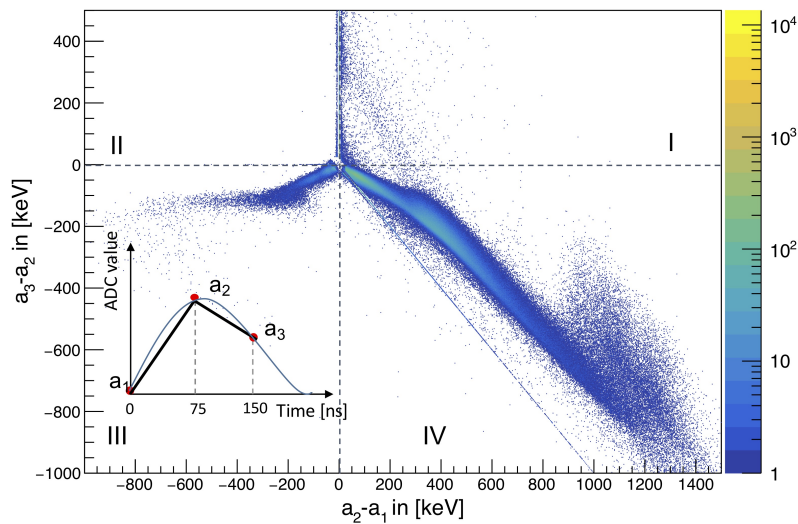


Figure 4.4: Plotted are the differences between the three samples against each other. The inset depicts a typical shaper pulse form with points of sampling. Valid events appear in quadrant IV. The pulse shape analysis identified 8% of the events as pile up.

5 Analysis and discussion

The analysis of the experimental data consists of several consecutive steps, which are summarized in Figure 5.1. At first, the raw data of the silicon detector are corrected for the different amplifier gain of the different APV chips. Here, the baseline and the band of signals at the range limit form a linear correction function. For energy calibration two special beam settings had been used. Here a proton with an energy of $E = 174$ MeV and the ^8He beam on empty target were used with a well known energy loss of $\Delta E_p = 92$ keV and $\Delta E_{^8\text{He}} = 397$ keV in $100\ \mu\text{m}$ silicon, derived from energy loss calculations of the empirical code ATIMA. For each individual APV, the position of the most probable energy loss in the energy spectra for both settings are determined. From these two points again a linear absolute energy scale is derived for the 3786 individual strips. The spectrum is then corrected by a factor so that the most probable energy loss is equal in all detectors. Afterwards, the aligned spectrum is absolute energy calibrated with calculations from ATIMA.

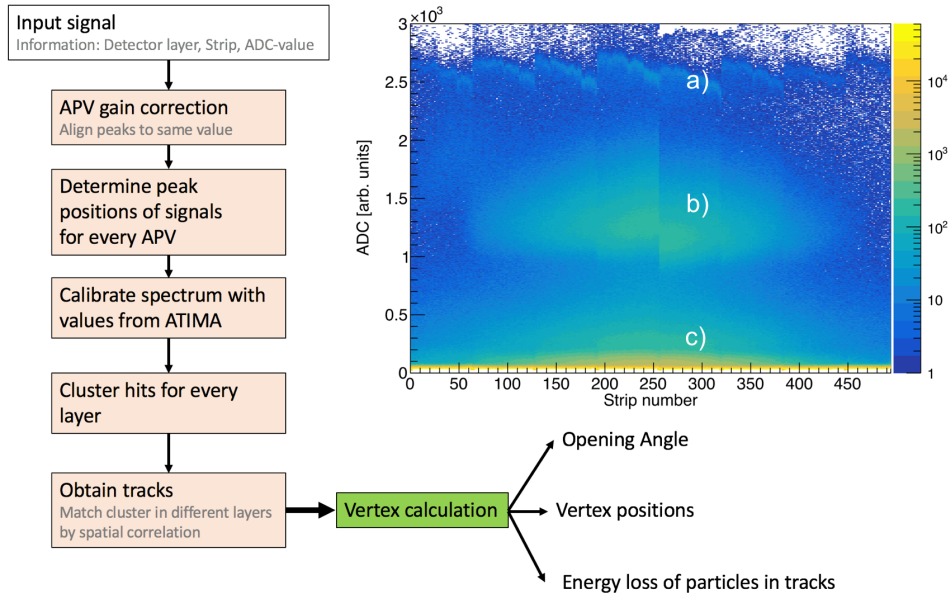


Figure 5.1: Schematic overview of the workflow for the track reconstruction. The inset depicts the raw energy spectrum for every strip in the first detector layer. a) Events with an energy loss that exceeds the range are shifted to the highest possible ADC value. b) The region with the most probable energy loss for the ^8He beam. c) Noise, crosstalk and distributed energy loss in neighboring strips are located in the low energy region. The amplifier gain is systematically different for every APV25 chip.

A clustering algorithm searches the calibrated data for clusters by looking for adjacent channels above a certain energy threshold. In the last step, tracks are obtained by matching clusters in the three different detectors modules in X and Y respectively. The obtained tracks are then used for vertex reconstructions to obtain observables such as opening angles, vertex positions and energy loss of the particles in the tracks. The individual steps of this procedure are discussed in detail in the following sections.

5.1 Energy calibration

The setup is optimized for the expected energy loss range of the particles in the silicon detectors, which is starting from 57 keV for high energy protons ($E = 400$ MeV) to more than 600 keV for slow α -particles ($E = 55$ AMeV). For energy calibration of all detector strips, two runs are used, where the target bubble was empty, just filled with nitrogen gas at a pressure of 800 mbar.

5.1.1 Amplifier gain correction

Since the gain for every APV chip is different, the mean energy loss is shifted systematically by blocks of 64 channels. The inset in Figure 5.1 depicts the energy loss of ^8He for every strip in the first detector layer. Clearly visible are small gain differences between every 64 channels/APV25 chip. Due to the limited range of 4096 channels of the APV25 chip, high energetic signals are moved to the same ADC value when exceeding the analogue range of the APV. ^8He deposits ~ 397 keV in 100 μm silicon as the most probable energy loss value.

The peak positions of these values are determined to correct for the gain factor. In the appendix, Table 7.1 depicts the fitted values for the peak positions.

5.1.2 Linear calibration

There were two different primary beam settings with significantly different energy deposit in the detectors available to calibrate the tracker as listed in Table 5.1 (see the calibration runs in the Figures 7.4 and 7.3 in the appendix). The deposited energy in a strip is directly

Particle	Energy [AMeV]	Energy loss in 100 μm Si [keV]
Proton	174	92.3
^8He	156	397.8

Table 5.1: Calculated energy loss for the beam particles in the calibration runs.

proportional to the ADC channel value. This is taken into account for the linear calibration function:

$$E_{\text{loss}}(x) = m \cdot \frac{1800}{c_{APV}} x + t \quad (5.1)$$

where x is the measured ADC-value, m is the slope of the fit, t is the offset and c_{APV} is an individual gain shift parameter, which is determined for every APV. The extracted values of the fit are $m = 0.1714 \text{ keV/ADC}$ and $t = 24.88 \text{ keV}$. The energy loss values for the calibration runs are obtained from ATIMA calculations. Due to the fact, that the calibration beams could not cover the full area of the detectors, an individual channel calibration was not performed here to avoid systematic effects. A rather homogeneous distribution of signal amplitudes as shown in Fig. 7.3 and Fig. 7.4 justified this procedure to be definitely sufficient to compare signals in different layers and separate Helium-like particles from single-charged ones. A plot of the calibration function is shown in Fig. 5.2.

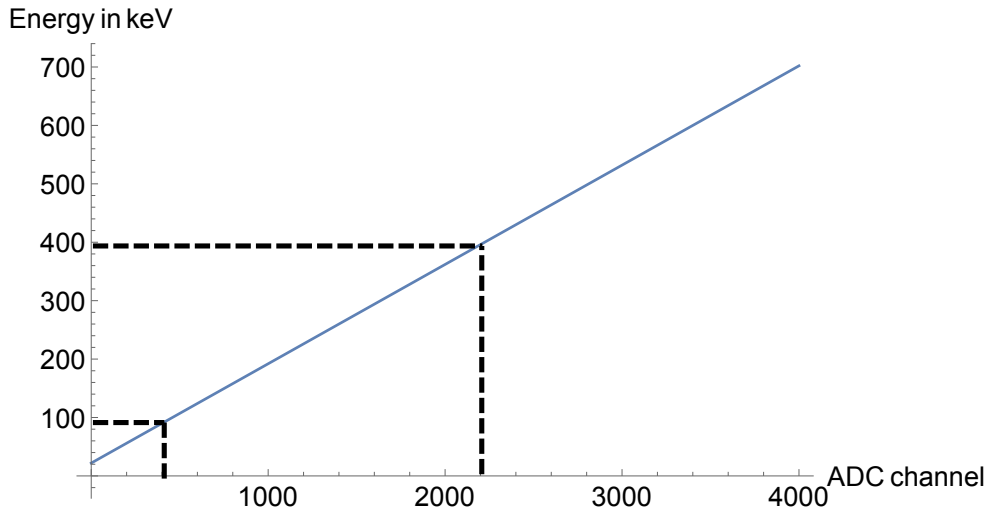


Figure 5.2: Plotted calibration correlation. The conversion is assumed linear. The calibration points of the empty target runs with proton and ^8He beam are indicated.

5.2 Clustering

Particles tend to deposit their energy not in a single but sometimes in several adjacent stripes. The energy loss is therefore split and can be reconstructed by summing the individual contributions. Adjacent stripes with a signal above the threshold are assumed to belong to the same particle and are called a cluster. The position x_{mean} of the penetrating particle is then determined by the center-of-gravity method:

$$x_{\text{mean}} = \frac{\sum_1^n x_i \cdot E_i}{\sum_1^n E_i} \quad (5.2)$$

where n is the number of adjacent strips above the threshold within a cluster, x_i is the position of the strip i and E_i is the energy signal in strip i .

In Fig. 5.3 the energy spectrum for the ^8He calibration run for the first detector layer (Y1) is shown before and after energy calibration and clustering. In the low energy range, the number of events is reduced by the clustering. Signals which exceed the APV25 range form several bands in the region $2100 < \text{ADC} < 2500$. The correct energy information is lost, and these events are considered as very slow particles with high energy deposit. The saw-tooth-like structure here corresponds to the individual offsets of each APV25 chip and a typical pattern of this within each chip.

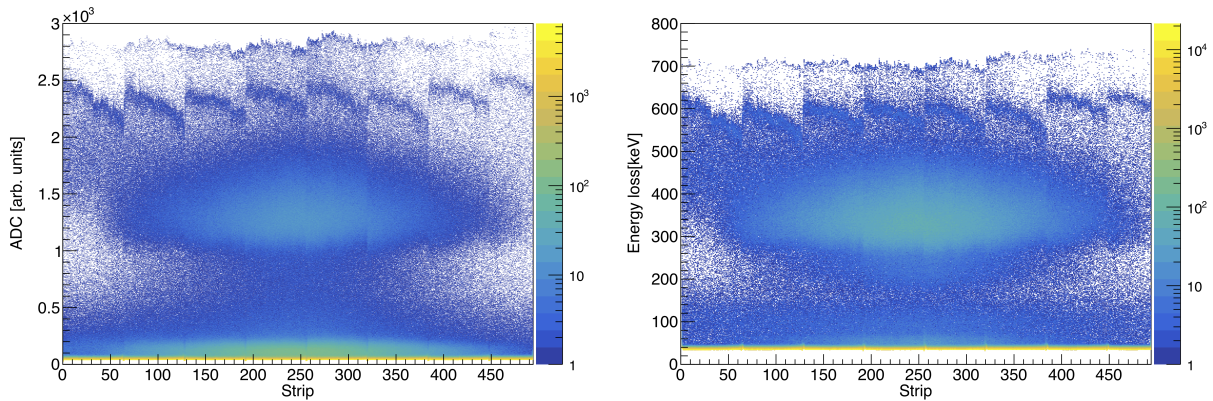


Figure 5.3: Left: Uncalibrated energy spectrum for the third detector layer. Right: Calibrated, corrected and clustered energy spectrum for the third detector layer. The prominent feature at ~ 300 keV to 400 keV is the energy loss of the ^8He particles in the wafer. The lower band at 100 keV is attributed to scattered protons. The low energetic noise in the uncalibrated spectrum is almost completely removed.

5.3 Track selection

Following the procedure in Figure 5.1, the next step is to reconstruct tracks from the particle hits (clusters) in the individual silicon layers.

To form individual particle tracks the three layer of each dimension (X and Y) are treated independently in a first step. Combinatorial samples of hits in all three layers are used to form all possible tracks for each X and Y. At higher multiplicities, this will contain a significant number of wrong assignments.

A simple combination by similar energy values is not possible due to the large energy spread for small signals and would lead to many wrong track assignments. Therefore, we take advantage of the three layers of silicon detectors and compare the flight directions of particles between the first two and the last two layers for each coordinate separately (see Fig. 5.4). When a particle travels through the detector on a straight line, the change in measured coordinates between the third and the second detector module should be equal to the difference between the coordinates in the second and the first layer. This is especially

true as the mechanical distances between the layers are equal with an accuracy of better than $\frac{\Delta z}{z} < 2 \times 10^{-3}$. Events, which fulfill this requirement are located on the correlation line.

Tracks with the wrongly chosen hit in the second detector layer are located on the anti-correlation. The tracks located on the horizontal and vertical line are randomly correlating a real hit with low signals, which are not cut by the threshold. Especially the first and last channel of each APV chip tends to produce such signal from electronic noise. Since the APVs are located directly behind each other, a fake track which is produced by them has a coordinate difference $\Delta X_{21,32}$ of zero between either the first and the second or the second and the third layer. This track in one part of the detector is then combined with an arbitrary track in the other part. To select physical events a cut on the correlation is then applied (see Fig. 5.4), which removes all fake tracks.

For vertex reconstruction, only straight tracks are useful. Additionally visible next to the primary correlation are smaller correlations shifted with an offset. These are related to crosstalk among the strips during the readout. The output multiplexer of the APV sorts the input channels not consecutively but in a binary coding where always ch_{i+32} follows after ch_i . Large signals can influence the information of the readout neighbors. This happens in all detector layers.

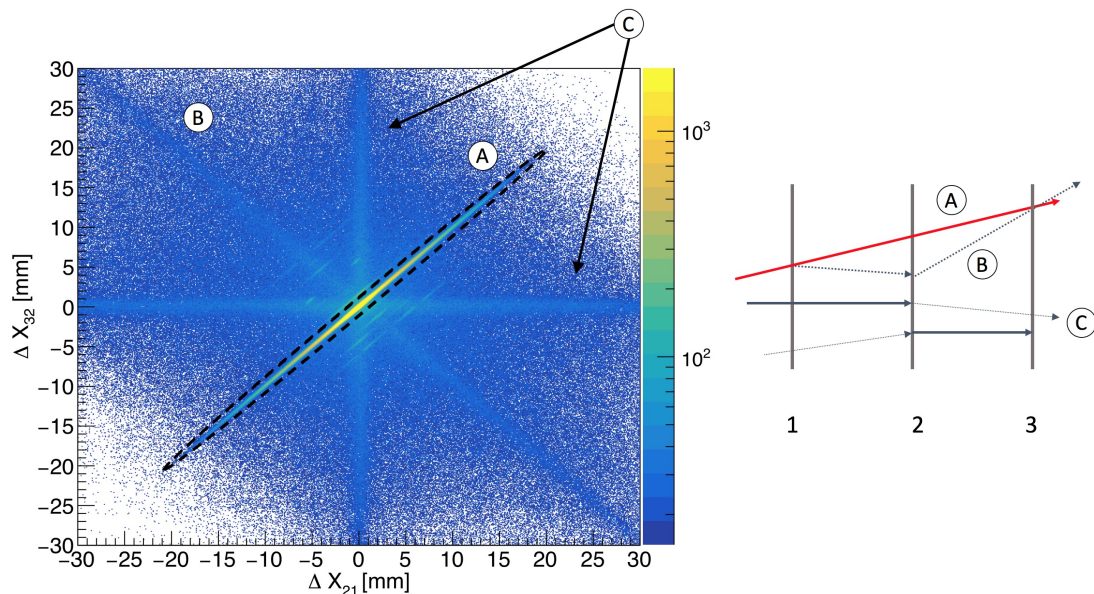


Figure 5.4: Left: ΔX_{32} plotted against ΔX_{21} . The events located on the correlation are straight particle tracks (A). The plot also shows anticorrelations due to scattering and mismatches (B and C). The selection on the correlated tracks is indicated in black.

The applied cut disregards all events, where the difference in coordinates exceeds 1 mm. The multiplicity of tracks per event is then shown in Figure 5.5. In most of the events, only one straight track is found. Multiplicities of up to nine tracks per event are possible in the tracker. In $\sim 28.6\%$ of events, no straight tracks can be found. The SBT trigger level was already downscaled due to a high sensitivity. Even for particle signals, which were

not focused in the preferred beam direction downstream and perpendicular to the detector planes, the trigger was activated. The X- and the Y-detector module have a small distance of 4.7 mm to each other only. To combine both pieces of information in a single hitpoint, the X strip information is linearly interpolated in Z-direction onto the Y-layer.

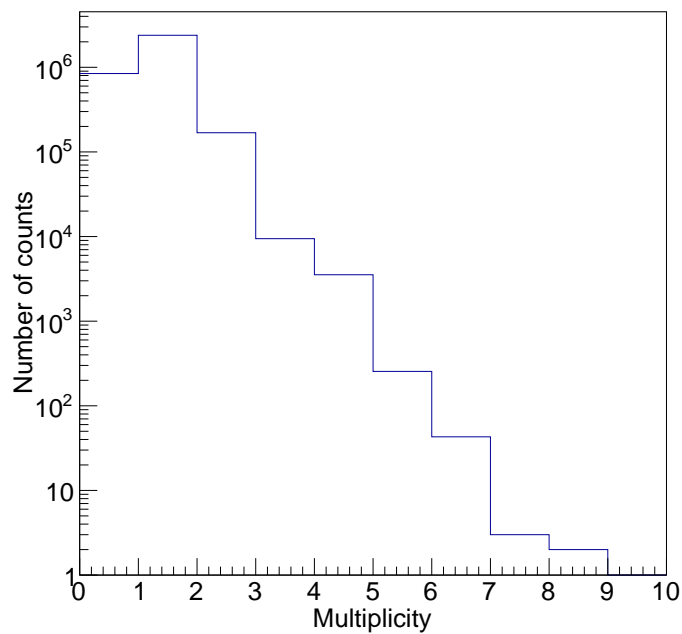


Figure 5.5: Multiplicity of tracks per event in the tracker.

5.4 Angular resolution

The angular resolution is an indicator of how strong particles are deflected in the detector and how well the detector can resolve this. It is crucial for the determination of the excitation energy as shown in Chapter 3.1. In the small angle approximation, it is defined in the tracker as:

$$\Delta\theta_c = \frac{\Delta C_{32} - \Delta C_{21}}{Z_3 - Z_1} \quad (5.3)$$

where ΔC_{ij} is the coordinate difference (x,y) between the detector layers i and j. The difference of the change in coordinates is normalized over the length of the tracker is shown in Figure 5.6 with a gaussian fit indicated in red. The extracted width is 136.0 μm for x and 154 μm for y with an statistical error of 2.33×10^{-5} and 2.73×10^{-5} . We obtain therefore for the angular resolution 0.56 mrad and 0.64 mrad respectively. The upper limit on the error is estimated to 1%. The total possible error on the angular resolution for a full target run with a ^8He -beam is:

$$\Delta\theta = \sqrt{\Delta\theta_x^2 + \Delta\theta_y^2} = (0.85 \pm 0.01) \text{ mrad} \quad (5.4)$$

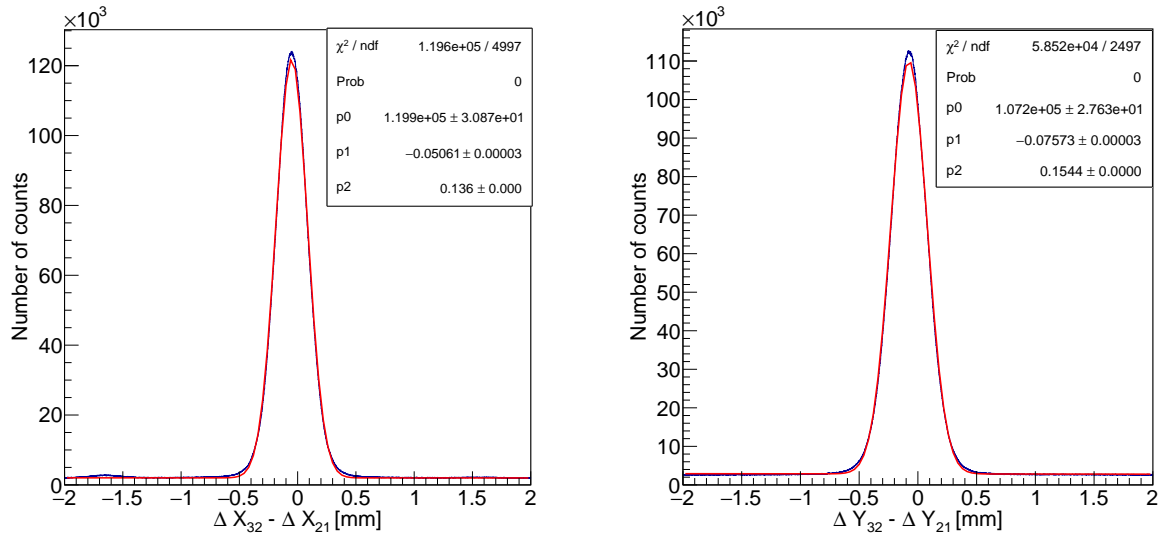


Figure 5.6: Left: Change in the x-coordinate for particles travelling through all layers. A standard deviation of 0.136 mm is obtained. Right: Change in the y-coordinate. The standard deviation is 0.154 mm. The value is divided by 24 cm to obtain the angular resolution.

5.5 Vertex reconstruction

The final goal of the silicon detector setup is to determine the position of the reaction vertex with high precision. After identifying particle tracks in the detector, the next step consists of determining the point of closest approach. The tracks in every event are combined with each other to reconstruct a vertex. Due to the limited precision of the detector resolution, the calculated tracks will never cross each other in a single point. They are always skewed to each other. The point of closest approach can, therefore, be considered as the reaction vertex.

The tracks are built as a combination of a position in space and a direction vector:

$$\begin{aligned}\vec{r}_1 &= r_{0,1} + \mu \cdot \vec{v}_1 \\ \vec{r}_2 &= r_{0,2} + \lambda \cdot \vec{v}_2\end{aligned}\tag{5.5}$$

where \vec{r}_i is the track, on which the particle moves, r_{0i} is the hit-position in the first detector module, \vec{v}_i is the normalized direction as a three-vector and λ or μ are parameters to form a straight line, with i being either 1 or 2. The connection vector \vec{d} between both tracks is given by:

$$\vec{d} = \vec{r}_2 - \vec{r}_1 = r_{0,2} - r_{0,1} + \lambda \cdot \vec{v}_2 - \mu \cdot \vec{v}_1 = \vec{r} + \lambda \cdot \vec{v}_2 - \mu \cdot \vec{v}_1\tag{5.6}$$

with $\vec{r} = r_{02} - r_{01}$. The squared length of this vector is:

$$|d|^2 = r^2 + 2\vec{r} \cdot \vec{v}_2 \lambda - 2\vec{r} \cdot \vec{v}_1 \mu - 2\lambda \mu \vec{v}_2 \cdot \vec{v}_1 + \mu^2 + \lambda^2\tag{5.7}$$

The derivatives with respect to the parameters are given by:

$$\begin{aligned}\frac{\partial(|d|^2)}{\partial \lambda} &= 0 = 2\vec{r} \cdot \vec{v}_2 - 2\vec{v}_1 \cdot \vec{v}_2 \mu + 2\lambda \\ \frac{\partial(|d|^2)}{\partial \mu} &= 0 = -2\vec{r} \cdot \vec{v}_1 - 2\vec{v}_1 \cdot \vec{v}_2 \lambda + 2\mu\end{aligned}\tag{5.8}$$

They are set to zero to find their values for the minimum distance between both tracks.

$$\begin{aligned}\lambda &= \mu \vec{v}_2 \cdot \vec{v}_1 - \vec{r} \cdot \vec{v}_2 \\ \mu &= \lambda \vec{v}_2 \cdot \vec{v}_1 + \vec{r} \cdot \vec{v}_1\end{aligned}\tag{5.9}$$

Solving now for λ gives :

$$\lambda = \frac{(\vec{r} \cdot \vec{v}_1) \cdot (\vec{v}_2 \cdot \vec{v}_1) - \vec{r} \cdot \vec{v}_2}{1 - (\vec{v}_2 \cdot \vec{v}_1)^2} \quad (5.10)$$

Since μ is a function of λ , one can calculate the two points on both tracks, where the distance between both tracks is minimized. Inserting both parameters in equation 5.7 and taking the square root, one obtains the minimum distance or distance-of-closest-approach (see Fig. 5.7).

The vertex is located in the middle on the minimized connection vector \vec{d} .

The majority of events have a DCA smaller than 0.2mm with a S/N better than 1. Events with a DCA larger than 0.2mm are not considered. This approach shows to clear out mismatched hits and is therefore similar to gating on the correlation as shown in Fig. 5.4. Additionally, it reduces the mismatch of X-tracks and Y-tracks to some degree.

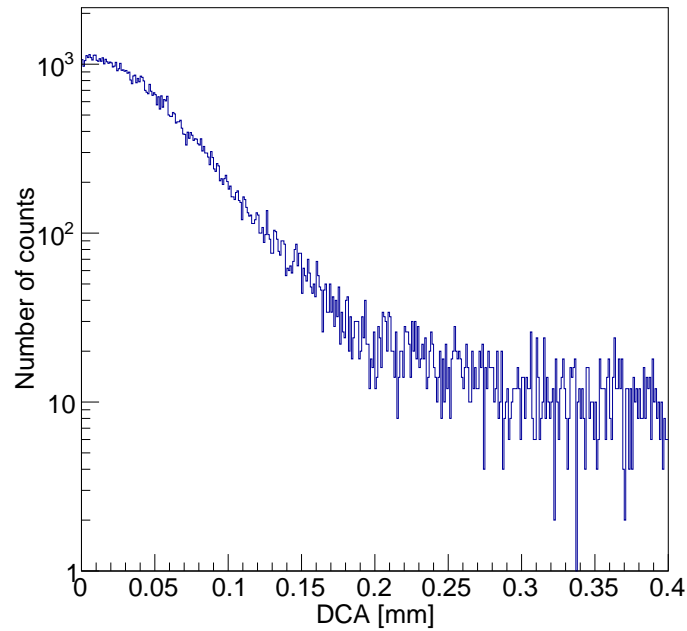


Figure 5.7: The distance-of-closest-approach (DCA) plotted for vertices reconstructed from a full target run.

5.6 Target reconstruction

The vertex reconstruction is optimized for the target region. For absolute position and resolution determination, it is important to compare widths and positions of known structures with reconstructions from the measurements. During runs with an empty target, the only material in the beam line with known widths and extensions is the target container. As discussed in Section 2.2 this is a bubble like transparent unit made from 120 μm Mylar. Particles are reacting with the bubble material, and the shape of the bubble is reconstructed with the vertex method. This allows determining the relative resolution as a function of the opening angles of the reaction as well as the distance to the tracker. After the resolution and the absolute positions are determined, the approach will be generalized to full target runs to determine the vertex point in the target.

5.6.1 Empty target reconstruction

During runs, where the target bubble is not filled the beam can only interact with the nitrogen replacement gas in the bubble or the material in the bubble tip. The target container's overall shape is cylindrically formed. The tip is a curved surface and not flat. Figure 5.8 shows the positions of the reconstructed vertices in 3D for the empty target run. In this representation, the z -coordinates are positive. The front tip (beam exit) of the target is located at small z while the backside (beam entrance window) is located at a z of ~ 60 mm. For larger z , the metal support structure of the bubble is visible at negative y . Since the target was filled with gas during empty target runs, several vertices are also reconstructed inside the bubble area. To determine the absolute position and the resolution of the tracker, the tip is fitted with a quadratic function, and the shape is corrected. Figure 5.9 shows scatter plots of the reconstructed target tips with and without quadratic correction. The z -position of the vertex is plotted against R , which is determined by:

$$R = \sqrt{x^2 + y^2} \tag{5.11}$$

The first detector layer is located at $Z \sim 0$ mm. Clearly visible is the bent shape of the tip at $z \sim -5$ mm, as well as the backside of the target bubble at $z \sim -55$ mm. Both the front and back side of the bubble have a similar width. As can already be seen in this figure, the uncertainty grows with more considerable distances to the detector. This is related to the lever arm of the vertex reconstruction and hence the multiple scattering in the material layers as well as the granularity of the detector.

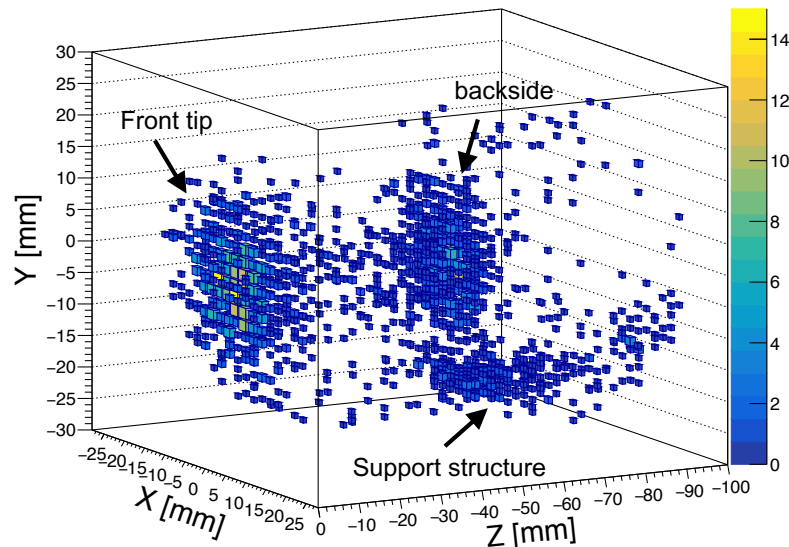


Figure 5.8: Reconstructed vertex positions in 3D for the empty target runs. Excess of vertices are visible in the front and back of the target and resemble the mylar enclosure shape. On the backside, the target's support structure is visible.

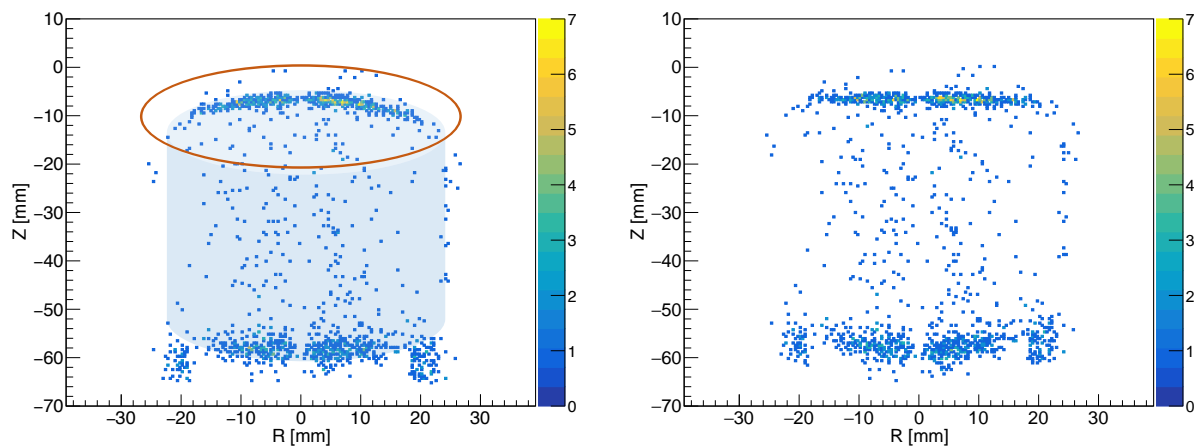


Figure 5.9: Left: Tomography of the empty target bubble. The Z position of the vertex is plotted against R. The bubble is marked by the blue overlay, and the brown circle indicates the tip. The bent shape of the target tip is visible. Right: Tomography of the empty target bubble with a corrected shape of the tip.

5.6.2 Absolute position and resolution

The distance between the first silicon detector layer and the target tip is referred to as the absolute position. It is crucial for the determination of the absolute vertex position in the target. During construction of the experiment, this safety distance was set to be in the range of ~ 5 to 6 mm with precision of several millimeters to prevent heat transfer from the APV chips on the silicon detectors to the target bubble by inserting an additional reflective foil (see Fig. 3.9). After employing all the known absolute positions of the silicon layers, the location and width are determined by vertex reconstruction. Figure 5.10 shows the projection of the corrected target tip with a gaussian fit. With the first detector layer being located at $z = 0$ mm, the mean position of the gaussian is the relative distance to the detector. A value of -6.75 mm is obtained.

The width of the fit is an indicator for the spatial resolution of the tracker. It is determined to 0.68 mm (Sigma) and therefore 1.47 times better than the expected constraint as discussed in Chapter 3.1. The true width of the target container is only $120 \mu\text{m}$, while the measured value is ~ 5.7 times larger. This is due to contributions from scattering as well as the extrapolation with small opening angles of the reactions. The measured width $w_{\text{meas.}}$ can be decomposed into the different contributions:

$$w_{\text{meas.}} = \sqrt{w_{\text{tip}}^2 + \Delta_{\text{scat.}}^2 + \Delta_{\text{det.}}^2(\theta)} \quad (5.12)$$

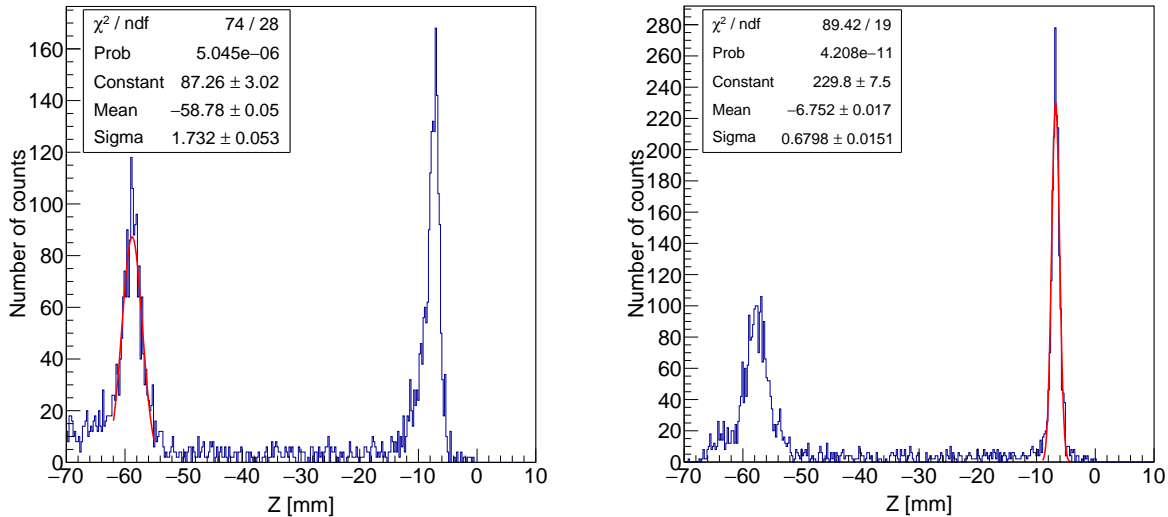


Figure 5.10: Projection of the empty target onto the z-axis with gaussian fit on the target backside ($\sigma_z = (1.73 \pm 0.05)$ mm) (left) and the target frontside ($\sigma_z = (0.68 \pm 0.02)$ mm) (right). The fitted projection is centered around ~ -6.8 mm (frontside), -58.8 mm (backside) and defines the absolute position of the target container's start and endpoint with respect to the first layer of the silicon detector.

where w_{tip} is the width of the target tip, $\Delta_{\text{scat.}}$ is the contribution from scattering in the silicon and $\Delta_{\text{det.}}(\theta)$ is the angular dependent part, which is related to the spatial extension of the strip.

5.6.3 Dominating contributions

The opening angle of the reaction has a direct impact on the spatial resolution of the detector (see Fig. 5.11). Due to the width of the strips, a $\tan^{-1}(\theta)$ dependency is expected. Additionally, particles coming from reactions with a small opening angle can penetrate the same channel in the first detector layer and can't be distinguished any more. Since the spatial resolution in z-direction σ_z is scaled by $\tan^{-1}(\theta)$ with respect to the x- and y-directions perpendicular to the beam axis, the overall spatial resolution can be assumed to be σ_z .

Figure 5.12 depicts the spatial resolution σ_z for different opening angles for the front and the end of the target. It is obtained by fitting the corrected shapes as described above. A clear trend to smaller resolutions for higher opening angles is visible. For reactions with tiny opening angles close to the detector, the fit breaks down due to limited statistics.

The uncertainty $\Delta_{\text{det.}}(\theta)$ for opening angles between 10° and 14° in the near vicinity of the tracker is:

$$\frac{100 \mu\text{m}}{\sqrt{12}} \cdot \tan^{-1}\left(\frac{10^\circ}{2}\right) = 330 \mu\text{m} \quad (5.13)$$

Already the effect of the detector granularity introduces an error contribution of around $330 \mu\text{m}$ for a particle track emitted with an opening angle of $\theta = \frac{10^\circ}{2}$. This effect dominates for small distances to the detector.

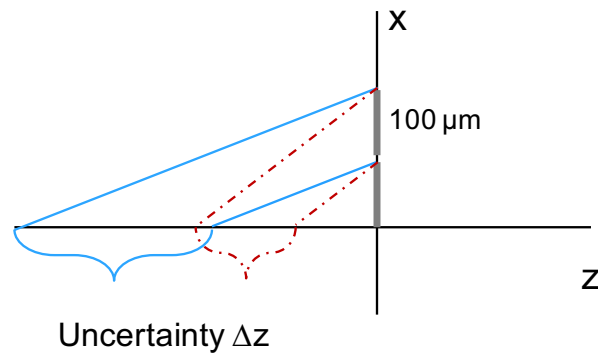


Figure 5.11: Sketch of the angular dependency of the z resolution close to the detector. Schematically drawn is the xz-plane with $100 \mu\text{m}$ strips of the detector. A particle crossing the strips with a small relative angle to the beam axis is depicted in blue. For reactions with larger relative angle, the uncertainty Δz shrinks (red dotted).

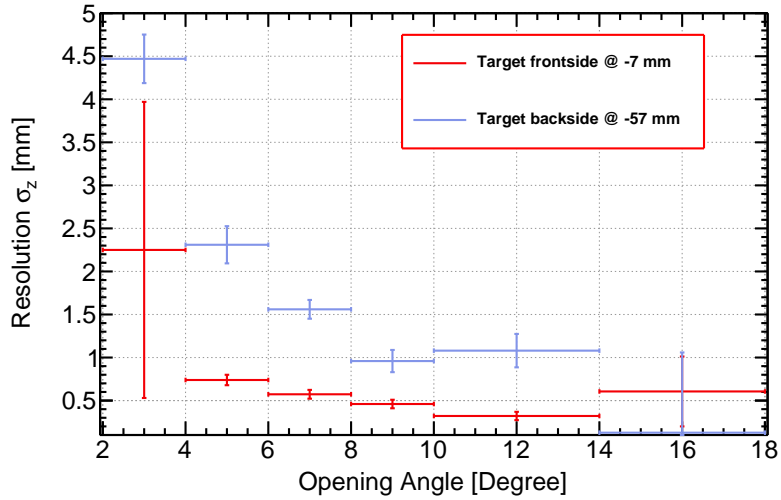


Figure 5.12: Measured widths of the target container in the front and at the back as a function of the opening angle of the reaction. In the front, the statistics breaks down for small opening angles.

The spatial resolution at larger distances to the tracker is mainly dominated by angular scattering. Protons and ^8He -particles with beam energies coming from the backside of the target ~ 50 mm introduce angular scattering by traversing the target's boundaries twice as well as the first silicon layer. This can be approximated to around 2 mrad. The uncertainty on the position in z for a fixed opening angle is therefore:

$$\Delta z = \frac{\Delta r}{\tan(\frac{\theta}{2})} = \frac{2 \text{ mrad} \cdot 50 \text{ mm}}{\tan(3.5^\circ)} = 1.6 \text{ mm} \quad (5.14)$$

where Δr is the uncertainty in the xy -plane on the first detector layer. This value is in excellent agreement with the measured width. However, the measured value is a product of different opening angles, particle combinations, and energies.

The minimized distance between target and detector optimized the resolution for vertices at a more extensive range. The resolution is then dominated by the angular scattering introduced from the target container or the liquid hydrogen respectively. For vertices, which are closely located, the resolution is governed by the effect of small opening angles. The opening angle distribution is expected to peak around 6° . Therefore, the contribution of this effect is only moderate.

5.6.4 Full target reconstruction

During the production runs the target bubble was filled with liquid hydrogen. The majority of reconstructed events is now located inside the target. The sum of all calculated vertices can be projected in the xz - and yz -plane as shown in Fig. 5.13. In the projection, the target has a length of ~ 50 mm as expected. A front view can be generated by plotting the x and

y components of the vertices against each other as in Fig. 5.14. In x- and y-direction, the vertices are gaussian distributed around 0 mm with a cutoff at ± 20 mm.

Figure 5.14 depicts the distribution of the vertices in the xy-plane. As discussed in Chapter 2.2 the target bubble has a diameter of around 4 cm. The spatial extension of the beam has a diameter of only 2 cm. The beam reacts mainly in this area with the target. In the ranges where x or y is larger than 10 mm edges and deformities coming from rescattering in the beam line and focus of the quadrupole magnets are visible. For vertices with a y-coordinate larger than 12 mm a cutoff is visible. This hints at a target bubble, which was not completely filled with liquid hydrogen. The void volume accounts for only $\sim 10\%$ of the whole volume. Also, the radial width of the beam is only 1 cm. The majority of reactions are therefore located in the radial center of the target.

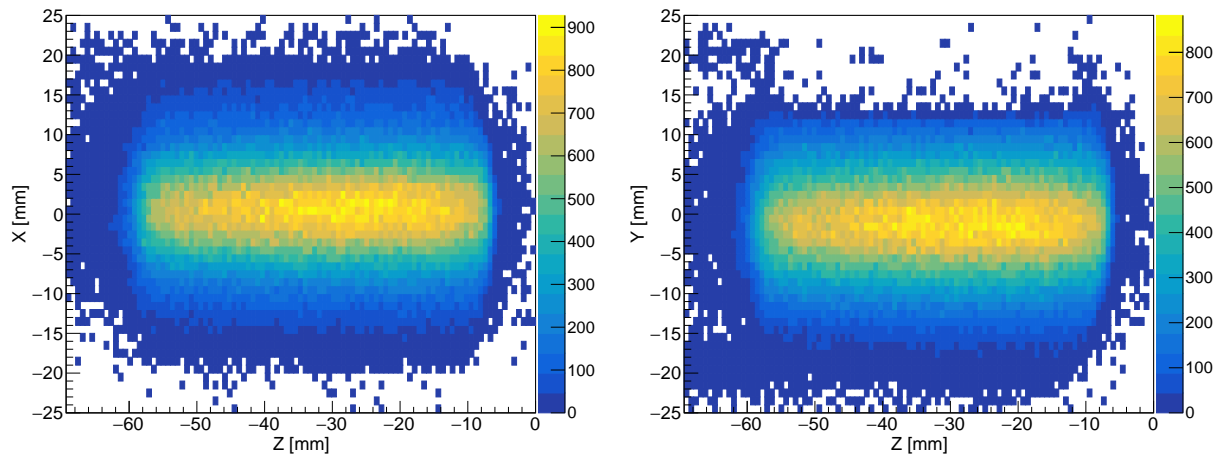


Figure 5.13: The xz-plane and yz-plane projection of the vertices are reconstructed in the target area for a production run. The cylindrical shape of the target is well visible. It is positioned between $z = -7$ mm and $z = -57$ mm, which matches with the target length of around 5 cm. In x, the vertices are peaking around 0 mm, which reflects the shape of the beam profile. There is a cutoff visible for vertices with $y > 12$ mm, which shows that the target bubble was not completely filled by LH_2 .

The target reconstruction can also be conducted by using the last two detector modules. In Figure 5.15, the vertex difference Δz between a reconstruction with the first and the second as well as with the second and the third detector layer is plotted against the opening angle θ of the reaction.

For large opening angles, the relative uncertainty shrinks as expected. For small θ , Δz can be as large as 15 mm. The large distance of more than 12 cm between the target and the second and third detector module leverages the error of multiple scattering in the target and the first detector module.

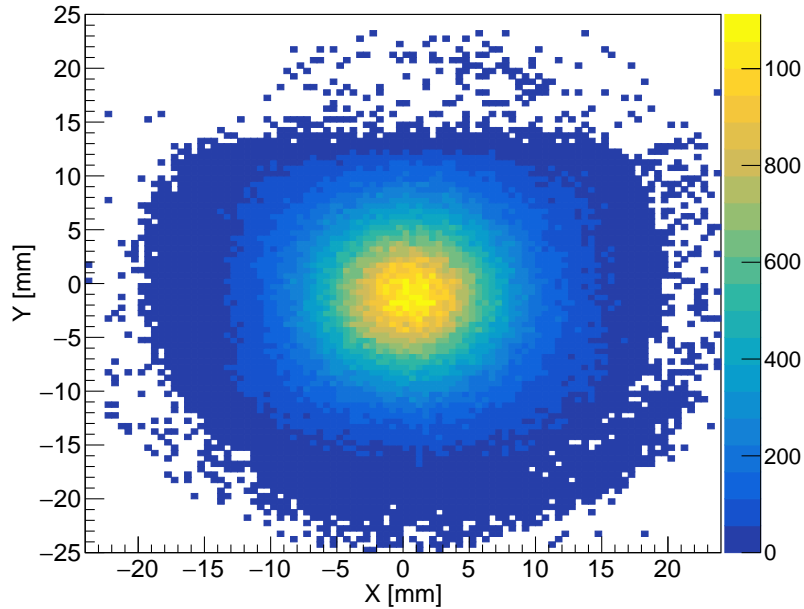


Figure 5.14: Projection of the x- and y-coordinates of the vertices in the target area. It indicates a well centered beam position and a partly filled target volume.

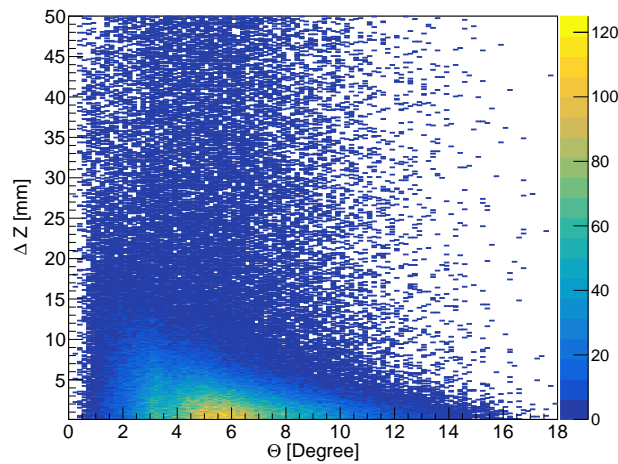


Figure 5.15: Δz resolution plotted against the opening angle of the two outgoing particles. The shape of the curve is expected to be proportional to $\tan^{-1}(\theta)$. The entries above an Δz of 20 mm are 10% random mismatches.

5.7 Detector efficiency

In general, the detection efficiency depends on the energy of the particle and the spatial acceptance but also on the electronics or inefficient areas of the sensor itself. We defined the specific detection efficiency for a single detector layer as the probability that a hit is registered in the layer at a particular position where a particle is expected to have passed the detector. This means if a particle with a certain energy loss was detected in layer one and two within a specific area, we also expect a hit to be seen in the extrapolated area in layer three. This efficiency excludes all other components, the overall dead time of the DAQ system, the trigger efficiency of the experiment and the angular acceptance of the setup. In this experiment, a high efficiency is essential to calculate the reaction cross-section and also to determine the performance of the detector with particles in different energy ranges. Spatial cuts are applied beforehand to select only events, where the particles traveled through the detector without substantial deflection.

The detection efficiencies for the proton and the helium calibration runs are shown in table 5.2. The efficiency error per detector layer is determined to 0.2% by varying the cuts. The overall detector efficiencies for the Protons at 174 MeV and the ^8He particles at 156 MeV are 83.7% and 84.8% respectively. The detector efficiency for the 400 MeV Protons is 83.6% and is obtained by linear interpolation.

The tracker detection efficiency is in an acceptable range. To raise the efficiency even further, one can ignore the information of one detector module, since it only provides redundant information to improve the signal-to-noise ratio. As the difference in efficiency between the Proton and Helium beam is rather small, a strong influence of the DAQ threshold is not likely. Other reasons for the inefficiency still have to be evaluated.

Detector	Efficiency Proton [%]	Efficiency Helium [%]
X ₁	96.2	96.9
X ₂	97.4	97.5
X ₃	96.2	96.9
Y ₁	97.3	97.3
Y ₂	98.1	97.8
Y ₃	97.3	97.3
All layers	83.7	84.8

Table 5.2: Efficiency of the detector layers for the proton and the ^8He calibration runs.

5.8 Event characterization

The energy loss of the tracked particles contains information of the reaction. Reconstructed tracks from the target area are related to particles, which are classified in types of low and high energy-loss particles. The energy loss of a single particle track in all six layers is averaged. After vertex reconstruction in the target, the energy losses of the particle tracks are ordered. In Figure 5.16, the averaged energies \overline{E}_{1-5} for particles with low and high energy losses are depicted. Several areas are marked, and two accumulation areas are visible (a) and b).

a) In the green marked area on the left side, both particles have a similar average energy loss of ~ 100 keV. Protons with an energy of $\sim E = 156$ MeV lose this amount of energy in one detector layer. It can be expected that these events originate from violent collisions where the ^8He -projectile entirely disintegrates.

b) In the red marked area on the right, the energy ranges from 60 keV to 150 keV for the particle with the low energy loss and 250 keV to 450 keV for the corresponding partner particle. This energy pattern fits the expectation from the ^4n production reaction with a slow α -particle with large energy loss in the silicon detectors and a fast proton with a small energy loss. However, the expected energy loss of the proton is only ~ 60 keV, while the α -particle should lose more than 500 keV. An elastic collision of the beam particle with a proton from the target is possible and would produce a similar pattern. The beam particle kicks out a single proton and accelerates it to beam energies at small transverse momentum transfer. The expected energy loss of the proton is then in the range of 100 keV to 150 keV. The relative change of energy of the beam particle is small, and therefore, the expected energy loss is with 390 keV relatively unchanged. Also, events, where the ^8He particle loses one or two neutrons in the collision and transforms into a ^6He , can produce this pattern.

c) Several events with one particle having an energy loss larger than 550 keV are also recorded. These events are related to extremely slow particles traversing the detector. The upper energy loss boundary of the detector shifts all events with an energy loss higher than 650 keV in this area. This gate also restricts the energy loss of the second particle to less than 100 keV. This pattern is more likely to be related to the ^4n production since the energy loss combination fits better. The amount of events in this gate is small since the number of production reactions is also expected to be low.

d) Well separated is the cyan band, where the particle with the low energy loss loses less than 50 keV. They are paired with a particle with an arbitrary energy loss between 80 keV and 650 keV. The low energy loss can't be explained by the fast protons produced in the reactions since the upper limit on the proton energy in the central knock-out reaction is around 400 MeV, which corresponds to the mean energy loss of 57 keV. It is more likely that these events are related to a pair of a hadronic particle with a delta electron. Delta electrons are also produced in the target and can be accelerated to few MeV, which would be sufficient to traverse the tracker in straight tracks without being deflected or absorbed.

A more thorough classification of the particles is only possible in combination with PID information from the HODOscopes.

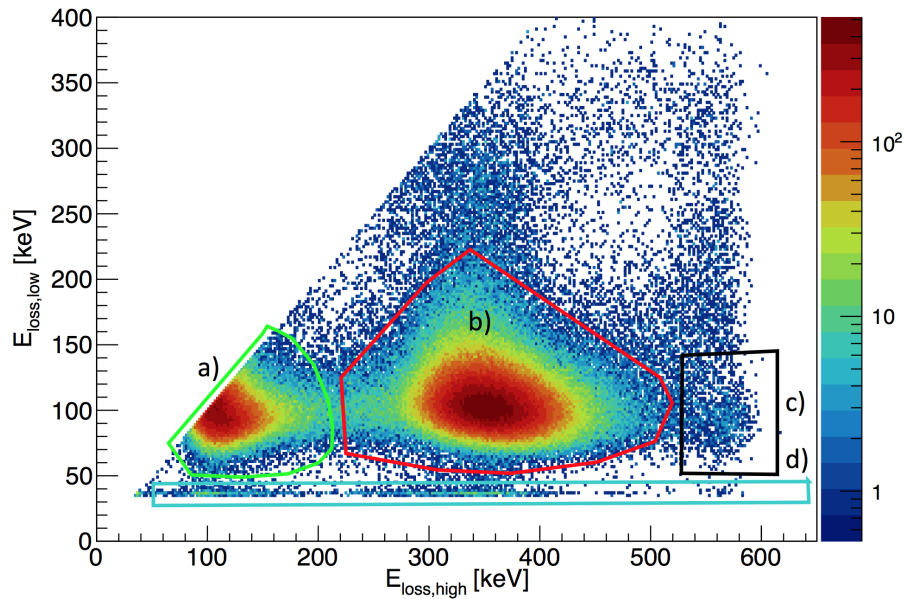


Figure 5.16: Energy loss of the identified particle tracks plotted against each other. The vertices are located in the target area. Four areas are selected. a) (green) In one type of reaction, both particles have a similar energy loss. b) (red) The majority of events consists of one particle having a small and the other having a high energy loss. c) (black) Combinations of one particle with intermediate to low energy loss and the other with very high energy loss are the purported area for the ^4n production reaction. d) (cyan) A well-separated band of events with one particle having an extremely small energy loss and the other one having a medium to large energy loss is visible below 50 keV on the Y-axis.

5.9 Angular pattern

A crucial aspect of the reaction is the angular distribution of the emitted particles. The opening angle can give hints on the type of reaction and therefore the nature of the emitted particles. The relative angles can show differences in the particle masses.

5.9.1 Relative angles to the beam axis

The relative opening angles of the reconstructed particle tracks to a hypothetical beam axis are shown in Figure 5.17. To further investigate the type of reactions, the gates on the particles' energies as shown in Figure 5.16 are used. Before the collision, the beam is pointing perpendicular to the detector planes. With good approximation, the transversal momentum of the beam particle can be assumed to be zero. The direction of the hypothetical beam axis is pointing perpendicular to all detector planes in beam direction. Due to the conservation of momenta, the transversal contributions must add up to zero again after the collision in a two-body kinematics. The detector measures the flight directions of the charged particles. The flight direction is in some sense proportional to the momentum of the particle. After the reaction, the momentum of a particle is $p_i = \sqrt{2 \cdot m_i \cdot E_i}$ in a

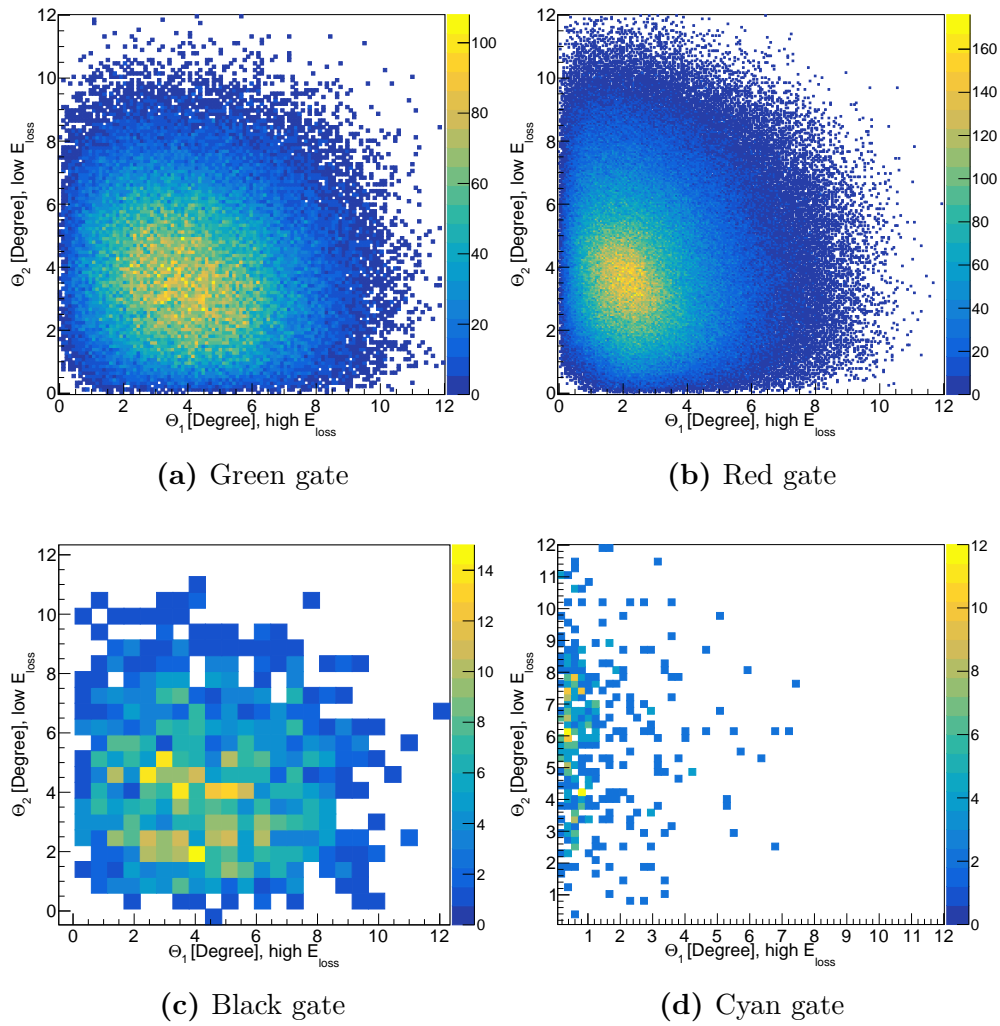


Figure 5.17: Relative opening angles to a hypothetical beam axis plotted against each other. Upper left: Both particles have similar energy loss and scatter with the same relative angle to the beam axis. Upper right: The particle with the higher energy loss is in general slower and tends to scatter under larger angles. Lower left: Broad distribution of relative opening angles. Lower right: The particles with the high energy loss scatters with low relative angles to the beam axis while the particles with the low energetic loss scatter under larger angles.

classical picture. Therefore, the momentum ratio can be approximated in the classical sense as:

$$\frac{p_1}{p_2} = \frac{\sqrt{2m_1 E_1}}{\sqrt{2m_2 E_2}} \quad (5.15)$$

a) Reactions, where both particles lost similar energy in the silicon detectors, show a similar relative opening angle of 4° to the beam axis. This hints at two particles with the same mass and energies. Protons produced in a spallation reaction, where the projectile breaks up can produce this pattern.

In b), the distribution is asymmetric. Particles with a larger energy loss tend to scatter to smaller relative angles ($\sim 2.8^\circ$) while particles with the lower energy loss are scattered to opening angles around 4° relative to the beam. The particle with the larger energy loss is, in general, the heavier particle. Since the transversal momentum is conserved, the lighter particle scatters to higher relative angles. In general, this type of signature can be produced by various combinations of a helium isotope which is produced by a neutron removal from the projectile in the collision and a proton. A possible candidate for this scenario is a ${}^6\text{He}$ particle, produced by neutron knockout and a proton. When the proton collides with an outer neutron of the ${}^8\text{He}$, it is accelerated to high energies. In this classical sense, the energy and mass combination of the charged products of the ${}^4\text{n}$ reaction is also a candidate. The particle energies for the ${}^4\text{n}$ production reaction are 55 AMeV for the α -particle and 400 MeV for the proton. Therefore, the momentum ratio is:

$$\frac{p_\alpha}{p_p} \sim \frac{\sqrt{2m_\alpha E_\alpha}}{\sqrt{2m_p E_p}} = 2 \cdot \sqrt{\frac{E_\alpha}{E_p}} \simeq \frac{2}{\sqrt{2}} = \sqrt{2} \quad (5.16)$$

The ratio of relative opening angles in Figure 5.17 is roughly $\sqrt{2}$. However, the energy loss of the α -particle should be much higher. A slight anti-correlation is also visible due to the impact parameter b in a collision between the proton and the ${}^8\text{He}$. For larger b , the proton is scattered under greater angles in the center-of-mass system. For smaller b , the change of the ${}^8\text{He}$ -angle is larger due to a stronger momentum transfer.

The black gate targets the region for the expected ${}^4\text{n}$ production. The distribution is broad and centered around 4° for both produced particles. A small anti-correlation is visible. Due to low statistics, a further investigation is not possible.

The distribution of relative opening angles for the cyan gate is showing an excess of events where the particle with the high energy loss is emitted with almost no relative opening angle to the beam axis, and the particle with the small energy loss tends to scatter at larger angles. This pattern underlines the assumption that these reactions consist of a hadronic particle and a delta electron, where the hadronic particle doesn't change direction in the collision, while the electron is scattered.

5.9.2 Opening angle distribution

The opening angle can be directly computed from the directions of the particles' tracks. Figure 5.18 shows the distribution of opening angles of the reactions in the gates in Figure 5.16. Very small angles are suppressed since they cannot be resolved at these distances between the silicon detector and the target. The suppression of larger angles is related to the angular acceptance of the detector. The opening angle distribution for the reactions in the green gate is shown in the upper left. The distribution peaks at $\sim 5-6^\circ$ and falls off gradually.

The Figure in the upper right corner depicts the opening angle distribution for the reactions in the red gate. The distribution is thinner than the one mentioned further and rises steeply with two maxima at $\sim 3^\circ$ and 5° and then falls off gradually. The 3° peak is thin compared to the maximum at 5° . The 3° anomaly is not expected, and it can be an indication for a reaction which favors an opening angle of 3° . An acceptance problem of the detector setup is also possible. To exclude the latter, the analysis is repeated for a different beam type.

Figure 5.19 depicts the distribution of opening angles for runs with a ^6He beam instead of a ^8He beam. The rest of the setup is unchanged. Instead of two peaks, only a plateau is visible between 3° and 6° . Otherwise, the shape of the distribution for large and small opening angles is similar. The absence of the 3° peak is another sign that this reaction is related to the ^8He -beam and the anticipated energy pattern.

In Figure 5.20, the opening angle of the reactions with ^8He is plotted against the relative angle of the reaction plane to the xz-plane. When the reaction plane angle relative to the xz-plane is small, events with a large opening angle can be detected. This comes from the fact that the detector modules are larger in x-direction than in y-direction. For large reaction plane angles, the reaction plane is oriented more and more perpendicular to the xz-plane. Small opening angles for reaction plane orientations of 0° and 90° are suppressed since in these cases, both particles end up in a single X or Y strip and cannot be distinguished anymore, leading to a multiplicity of one in the detector module. For all angles in the reaction plane, the distribution of the opening angles is broad with a peak at $\sim 4^\circ - 6^\circ$. Additionally, A small band is visible at 3° and is independent of the reaction plane angle. This shows that the opening angle is independent of the orientation of the reaction. An opening angle of three degrees is favored regardless of the orientation of the reaction plane. Therefore, it is unlikely that this is caused by an acceptance problem or the triggering detectors.

The excess at a rather small opening angle of 3° can be a sign for a preferred reaction involving ^8He . Since the surplus is located at a smaller angle than the maximum at 5° , the charged particles are emitted stronger in the forward direction. This is linked to a boost in the longitudinal direction. Binding energy of a few MeV released in the collision by the separation of neutrons could in principle lead to smaller opening angles between the charged particles by boosting them in the forward direction. However, the binding energy released is only a few MeV, which is too small to make an effect in comparison with the particles energies. It is also possible that this could be a p+He resonance. To have a

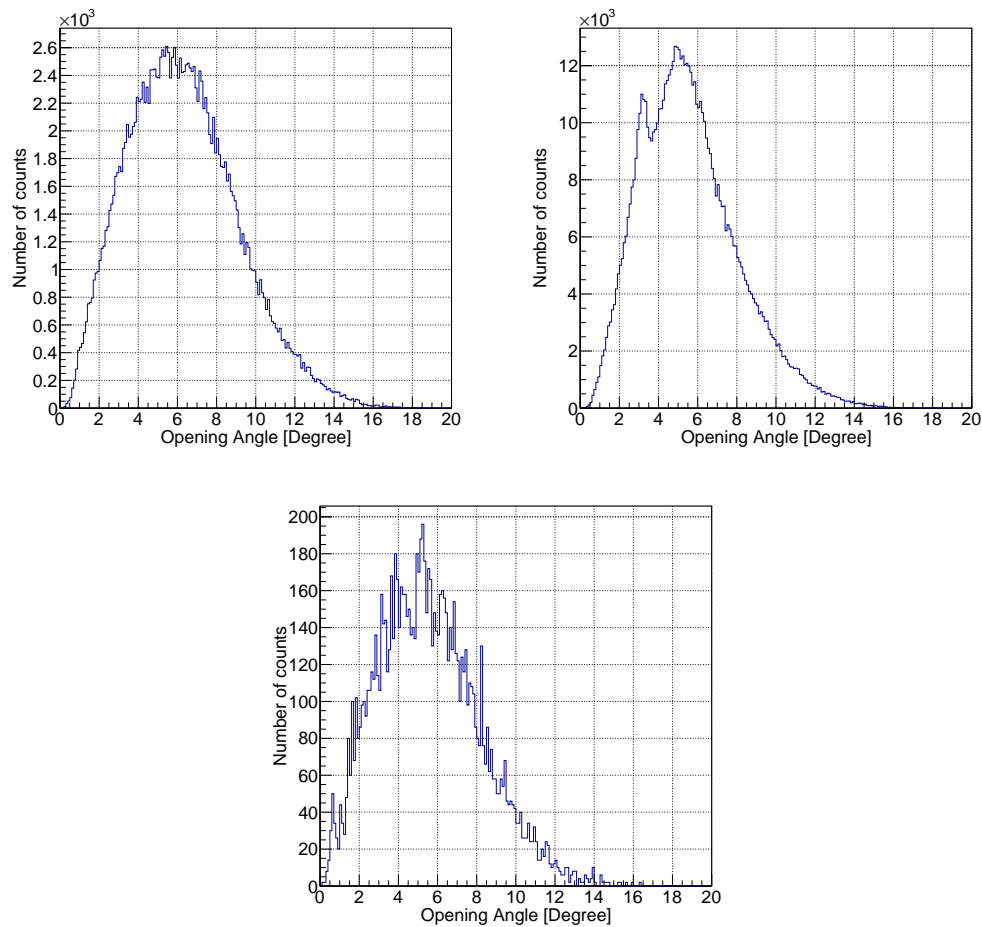


Figure 5.18: Upper left: Opening angle of charged particles in the green gate of Figure 5.16. The distribution peaks at $\sim 5^\circ$. Upper right: Opening angle of the reactions in the red gate (see Fig. 5.16). A smaller peak is visible at 3° . Down: Opening angle of reactions in the black gate (see Fig. 5.16).

final state interaction, the relative speed of the particles should be small. To understand this effect the particle identification and the energy and momenta measurement from the combination of the data with the other subdetectors is crucial.

Lastly, the opening angle distribution for the black gate is depicted. Due to a lack of statistics, a clear statement can't be made. However, the distribution seems to peak at 4° and 6° . The 4° peak is expected from simulations of the opening angle distribution [12] and hints at the production of ${}^4\text{n}$ in events with this energy characterization.

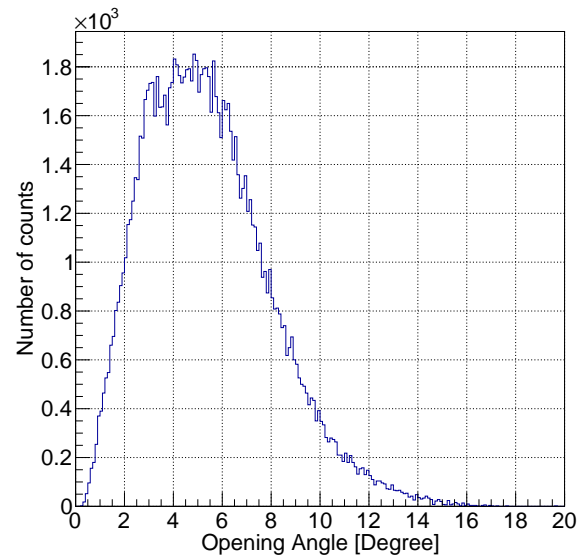


Figure 5.19: Opening angle of the charged particles for reactions with ${}^6\text{He}$.

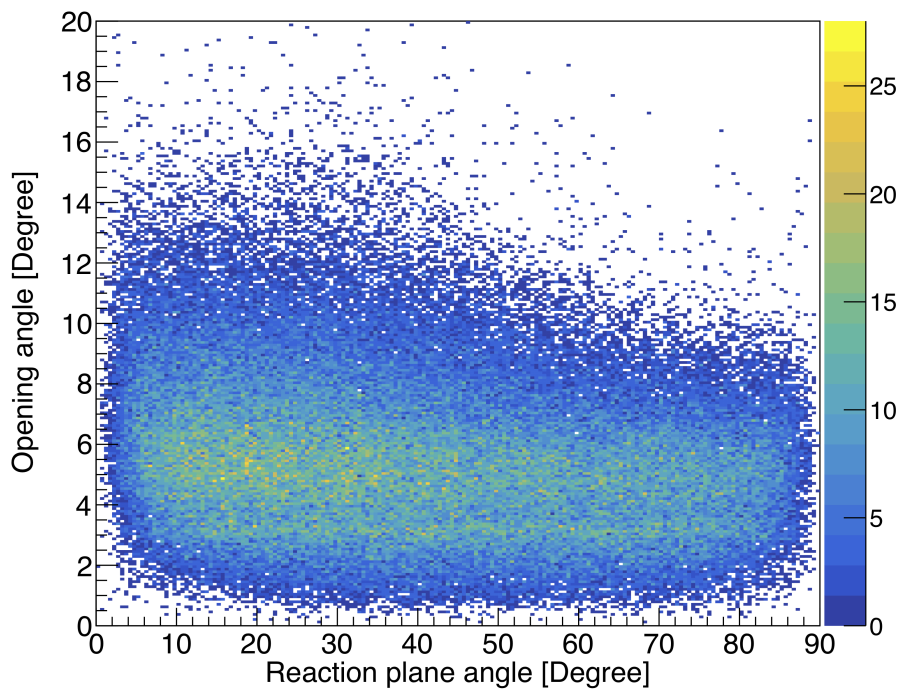


Figure 5.20: Opening angle plotted against the angle of the reaction plane. Events with a reaction plane angle of 0° and 90° have both particles leaving a signal in the same X or Y strip and are removed by the multiplicity cut. Since the detector plane is larger in x-direction than in y-direction, larger opening angles are suppressed with larger reaction plane angles. A thin band with an opening angle of 3° is visible for all angles of the reaction plane.

5.10 Out-of-plane transfer

The angular orientation of the beam particle with respect to the plane spanned by the two charged product particles gives hints on possible three-body reactions and out-of-plane momentum transfers (see Fig. 5.21).

After the reaction, the direction vectors of the two outgoing particles form a plane. The difference between the direction of the incoming beam particle and the plane can be investigated to observe a transfer of transversal momentum. Notably, the detector is only capable of measuring the flight directions of charged particles. The beam particle's direction is measured with the BDC in front of the target.

For a production of only two particles, the relative angle between the beam vector and the plane should be zero. In the case of three emitted particles, the beam particle can be tilted with respect to the plane, since a transversal momentum is passed to the third undetected particle.

The directions of incoming and outgoing particles are normalized. To calculate the out-of-plane angle, the direction difference between the beam particle and the charged particles is calculated:

$$\vec{t}_i = \vec{v}_i - \vec{v}_b \quad (5.17)$$

where \vec{v}_i is the direction of one of the charged particles and \vec{v}_b is the direction of the beam particle. The transversal angle is then the magnitude of the sum of \vec{t}_1 and \vec{t}_2 divided by two.

Figure 5.22 depicts the out-of-plane angle plotted against the opening angle.

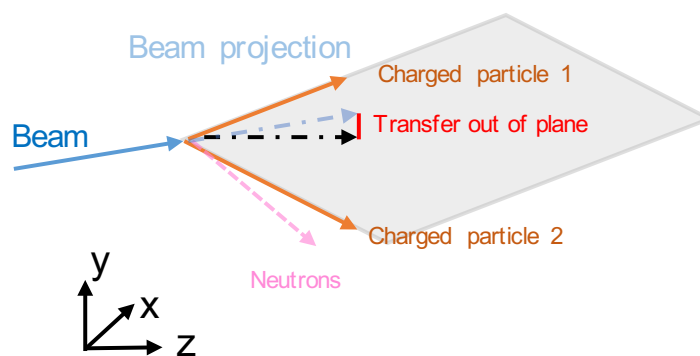


Figure 5.21: Schematic drawing of a three-body production. The produced charged particles are depicted in orange and define a plane. The beam particle is depicted in blue and is destroyed in the reaction. The black dotted arrow is the projection of the beam direction onto the plane. The undetected third produced particle is depicted in ping. The transversal difference of the beam particle with respect to the plane is shown in red.

- a) The out-of-plane transfer for the green gate is peaking around $2-3^\circ$. The distribution is broad and cut-off for large out-of-plane transfers or opening angles. This shows that there is a distribution of transfers out of the plane for any opening angle. This is expected for reactions with more than two particles in the outgoing channel since there is no correlation between the opening angle and the transversal angle.
- b) The out-of-plane transfer for the red gate is located at smaller opening transversal angles than compared to the events in the green gate (see Fig. 5.16). This means that the out-of-plane change of the undetected particles is smaller as in the case a) and also, that both charged particles and neutrons are more boosted into the forward direction. The 3° excess for the opening angle is independent of the transversal angle, even though there is a small excess at an out-of-plane transfer of $1-1.5^\circ$. Due to the small statistics, this is however not significant.
- c) The out-of-plane angle is half the opening angle. This is expected when the beam particle and one produced charged particle fly in the same direction. The beam particle is then located in the plane of the two outgoing particles. This is the case of reactions where delta electrons are produced, and no third undetected particle is emitted out-of-plane. The beam particle doesn't change its direction, but electrons are liberated in the collision with atoms.

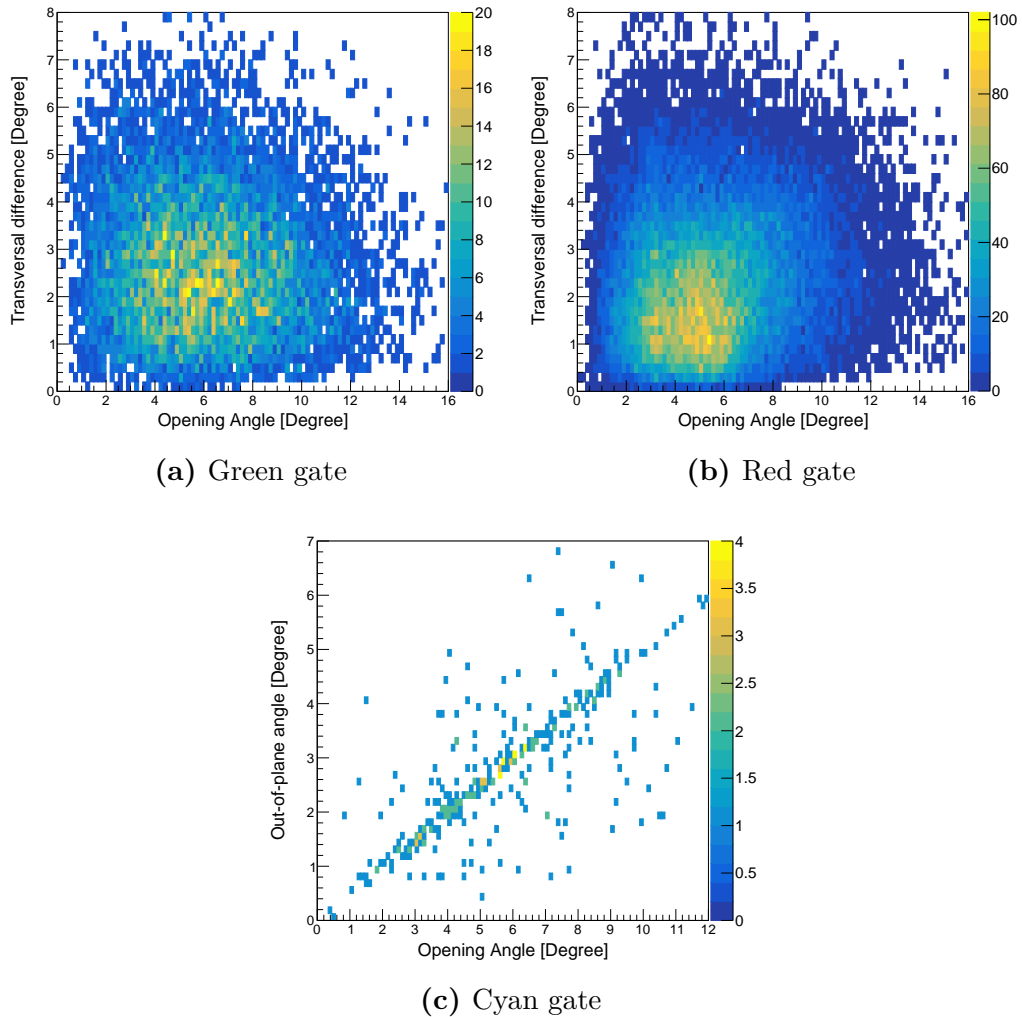


Figure 5.22: Out-of-plane angle plotted against the opening angle of the reactions for different reactions. Upper left: The transversal angle is around half the opening angle. The distribution is broadened due to the restricted resolution of the BDC. Upper right: The excess of events is located below the bisection. The excess of events with an opening angle of 3° is independent of the transversal angle. Lower: The out-of-plane angle is half the opening angle. This comes from the fact that one particle follows the beam direction while the other particle is emitted relative to the beam. Then the opening angle is twice the calculated transversal angle.

6 Summary and outlook

Multi neutron systems could contribute prominent information to the field of neutron-neutron interaction and the equation-of-state of dense neutron systems such as neutron-stars [21]. The tetra-neutron (4n) in particular is a hypothetical resonance state of four neutrons which is suitable to simulate neutron-neutron interaction in high-density environments, which are believed to exist in, e.g. neutron stars. Missing-mass experiments hint at a possible resonance at $M_{4n} \approx 0$ MeV but lack of sufficient statistics and exclusive measurements of the final state [11]. The SAMURAI19 experiments aims at producing 4n in the reaction ${}^8\text{He}(p, p\alpha){}^4n$ in inverse kinematics at beam-energies of $E_b = 156$ A MeV with a beam-rate of 200 kHz [12]. The 4n systems are directly measured in the NeuLAND and NEBULA detectors. To maximize the interaction rate, a 5 cm long liquid-hydrogen target (MINOS) is used [16]. The scattering of particles in the target is expected to dominate the anticipated missing-mass energy resolution of 1.6 MeV (FWHM).

This thesis described the development and performance of a novel high rate in-beam silicon vertex-tracker to minimize the uncertainty on the energy loss of charged particles in the target by determining the reaction vertex with resolutions better than $\sigma_z = 1$ mm and to measure the opening angle of the reactions with precisions better than 1 mrad. The tracker consists of six $5\text{ cm} \times 8\text{ cm}$ large single-sided X- and Y-silicon detectors, each with a thickness of $100\ \mu\text{m}$ and a segmentation of $100\ \mu\text{m}$. Two detectors are stacked in three newly designed XY-modules in a vacuum chamber. The first layer was placed only 5 mm away from the target to optimize the resolution of the vertex reconstruction. The setup can read out each channel individually several times per event via the ASIC chip APV25S1. The data is then processed via an ADCM-module to a single TRB3 board and forwarded into the RIKEN DAQ-system. Beam pile-up can be removed channel-wise with a sophisticated pulse shape analysis.

Analysis of the data shows that the detector reliably distinguishes between particles with high energy-loss of more than 550 keV and low energy-loss of only 40 keV. Track selection was employed by setting strict constraints on the straightness of tracks. The angular resolution has been determined to 0.84 mrad.

A vertex reconstruction of the empty target demonstrated a tracking resolution of $\sigma_z = 680\ \mu\text{m}$ in the front of the target to $\sigma_z = 1.7$ mm in the back. The angular dependence of the vertex resolution has been characterized. The granularity of the strip width dominates the resolution close to the detector while the resolution for events with a vertex far from the detector is dominated by multiple scattering in the target and the first detector plane.

The energies of reconstructed tracks originating from the target area have been analyzed. Several well-separated regions, which belong to different reactions were identified. The

relative opening angles for these reactions were investigated for further hints at the particle types. The ratio of relative angles depicts information on the momenta ratio. The out-of-plane angle between the beam particle and the plane created by the charged products was used to investigate momentum transfer to a third undetected particle.

The tracker exceeds all requirements from the proposal. To create a missing-mass spectrum of the ${}^4\text{n}$, the data has to be analyzed in composition with information from other detectors. The origin of the 3° anomaly is still unclear at this point. A particle identification of the involved charged particles will probably shine light on this.

The tracker proved its reliability and precision in this experiment. However, several points of improvement should be considered. The energy calibration can be highly improved in the range upwards from 400 keV by choosing lower-energetic particles so that a third reference point is available. Even though a strict DCA cut proved good performance on removing mismatches, mismatches of reconstructed tracks in X and Y can be removed by using timing correlation or replacing one detector module with a silicon pixel detector.

7 Appendix

7.1 Y layer

To realize a tracking in three dimensions, a new detector for Y-readout has been developed. Figure 7.1 depicts the concept drawing of the Y-PCB. The Y-PCB was designed as a modification of the X-PCB as used in [18]. 468 channels of 100 μm thick silicon strips with a length of 8 cm and a width of 100 μm are readout by 8 APV25 chips. The strips are connected to the ASICs by a pitch adapter. Figure 7.2 shows a picture of a Y-detector from above before bonding. The wafer is placed in a ceramic frame, which absorbs shocks to prevent the wafer from breaking.

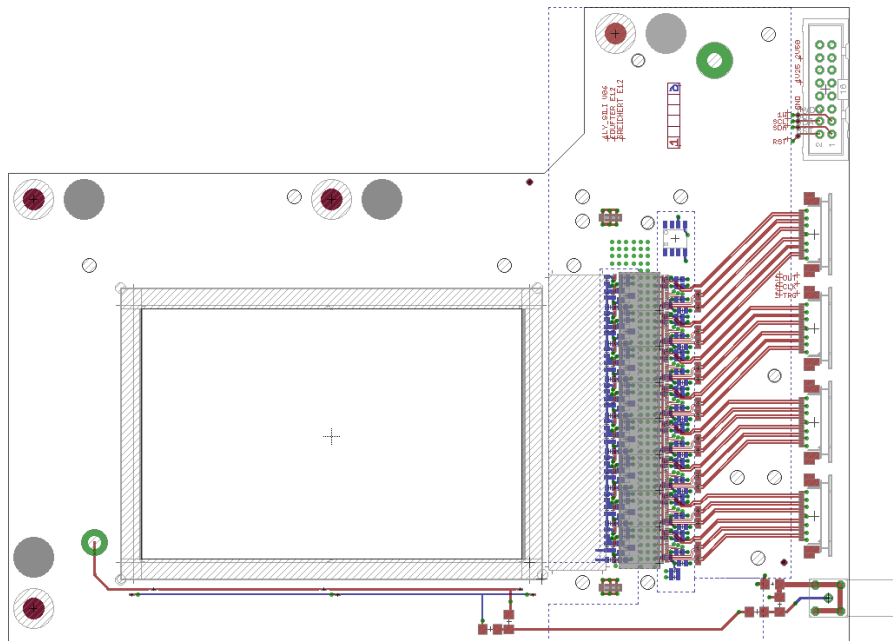


Figure 7.1: Schematic picture of the Y-PCB circuit. Data and power connections are depicted as red lines. Vias and breakthroughs are colored in green. Electronics on the back side are depicted in blue. The APVs are situated in the dark grey area and are read out to the right side. Additionally, a power supply for the APVs and the wafer is located on the top right and lower right side respectively.

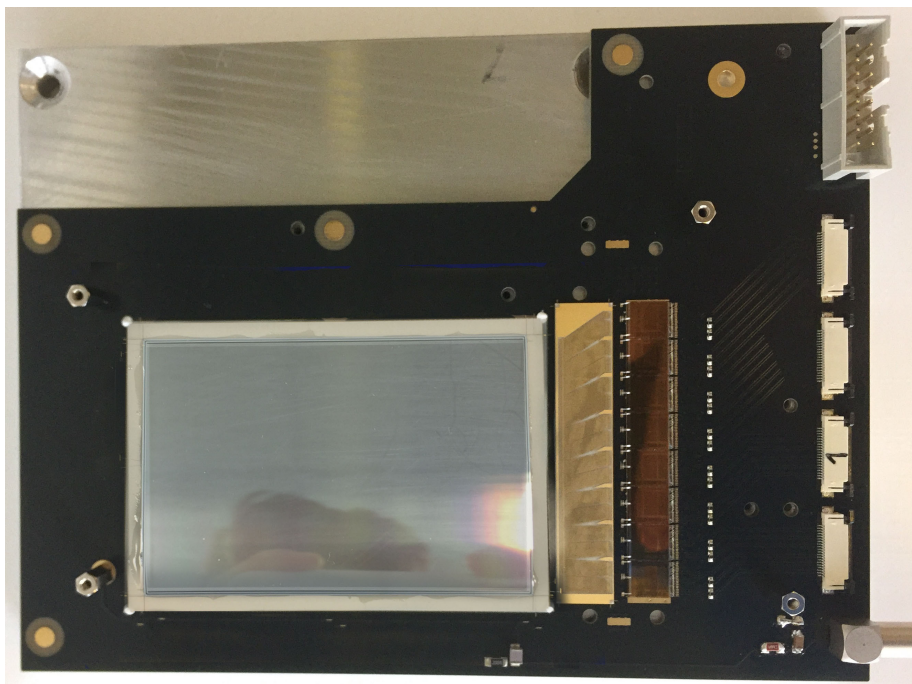


Figure 7.2: Picture of a Y-detector layer before bonding. The silicon wafer is placed on the ceramic frame and the pitch adapter as well as the APV-chips are connected to the PCB.

7.2 APV gain correction

Table 7.1 depicts the fitted mean landau peak position for every APV in the detectors for the ^8He calibration run. It is later used to align the mean energy loss over all APVs to a reference value, which is then fixed as the mean avg. energy loss of ^8He in $100\ \mu\text{m}$ silicon for $E_{beam} = 156\ \text{AMeV}$.

Detector	APV	Landau peak position [ADC channel]
Y1	1	1318
Y1	2	1268
Y1	3	1312
Y1	4	1308
Y1	5	1214
Y1	6	1206
Y1	7	1186
Y1	8	1156
X1	1	1382
X1	2	1335
X1	3	1335
X1	4	1324
X1	5	1358
X1	6	1312
X1	7	1268
X1	8	1298
X1	9	1308
X1	10	1335
X1	11	1290
X1	12	1335
Y2	1	1283
Y2	2	1283
Y2	3	1260
Y2	4	1286
Y2	5	1302
Y2	6	1254
Y2	7	1244
Y2	8	1283
X2	1	1342
X2	2	1342
X2	3	1342
X2	4	1354
X2	5	1284
X2	6	1338
X2	7	1318
X2	8	1314

X2	9	1328
X2	10	1342
X2	11	1342
X2	12	1342
Y3	1	1344
Y3	2	1344
Y3	3	1322
Y3	4	1274
Y3	5	1258
Y3	6	1306
Y3	7	1264
Y3	8	1264
X3	1	1312
X3	2	1312
X3	3	1312
X3	4	1336
X3	5	1262
X3	6	1250
X3	7	1322
X3	8	1280
X3	9	1352
X3	10	1324
X3	11	1312
X3	12	1250

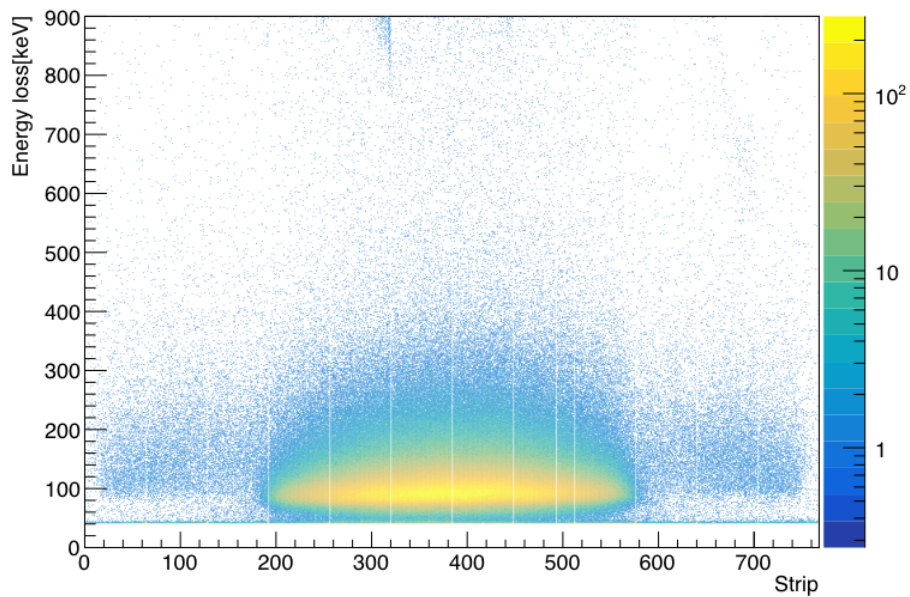


Figure 7.3: Calibrated and clustered spectrum of the first silicon layer for the proton calibration run. Depicted is the energy loss for every the strip. The majority of events are centered around the center of the detector.

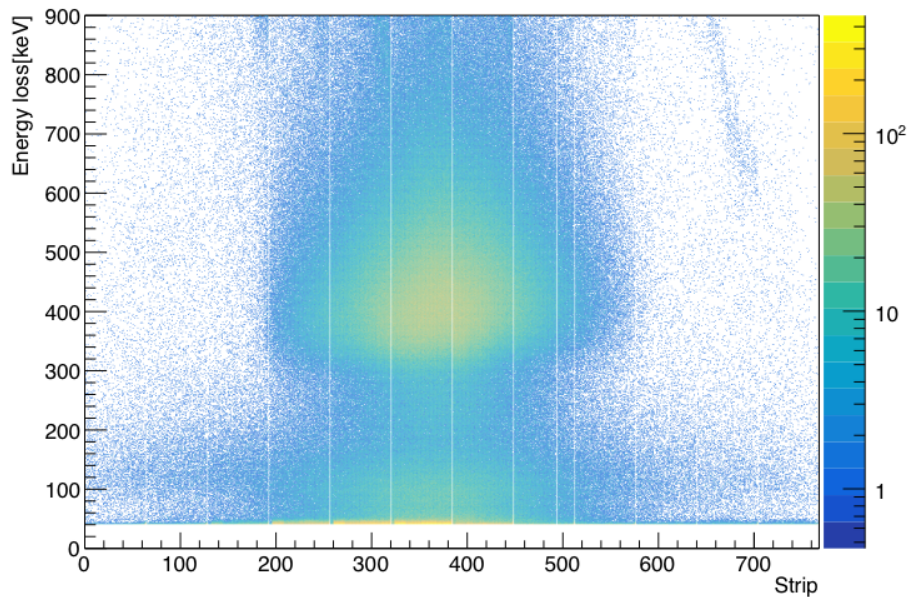


Figure 7.4: Calibrated and clustered spectrum of the first silicon layer for the ^8He calibration run. The mean energy loss is located at around 400 keV. The band at ~ 100 keV is related to protons accelerated in the collision with the beam.

7.3 Incompletely filled target

The target bubble was not always completely filled up with LH_2 . The beam extension is with around 2 cm smaller than the target's diameter of 2 cm. However, rescattered particles react in the areas further away from the beam extension cutoff. The form of the target is cylindrically shaped. Therefore a full cylinder is expected to be seen in the reconstruction. In several runs (e.g., 254, 255, 256, etc.) the target was only filled by $\sim 75\%$. This can be seen in the vertical cutoff of the reconstructed target (see Fig. 7.5). The target is only filled to a height of ~ 12 mm. In overall, this decreases the event statistics. The untouched area only represents 10% of the targets cross-section and the majority of beam particles is centered around ± 10 mm. During the runs, the temperature of the target bubble was measured to 21.51 K, which is close to the boiling threshold temperature. The temperature in the target can be raised above the threshold by defects in the insulation or emitted heat from the APV25 chips.

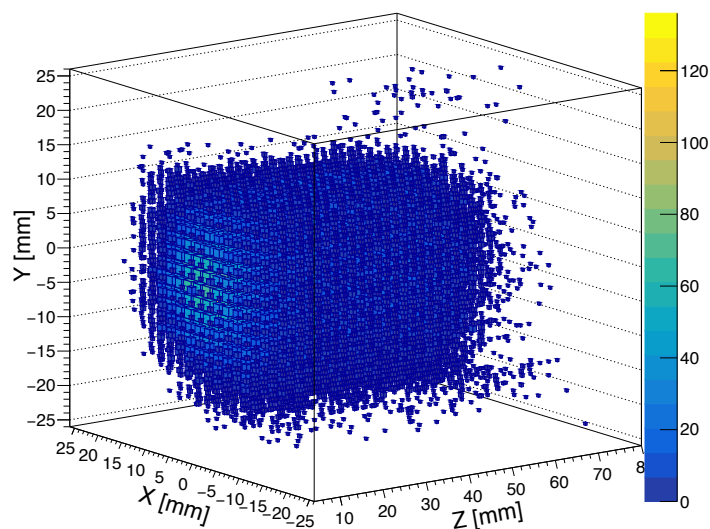


Figure 7.5: 3D picture of the reconstructed target from a full-target run.

7.4 Helium-6

During the experiment, the particle type of the beam was also switched to ${}^6\text{He}$ to take reference data at the same beam energy. The data of these runs were analyzed in the same way as the ${}^8\text{He}$ data to depict differences. Figure 7.6 for example depicts the relative opening angles to the hypothetical beam axis of produced particles coming from the target for the same gates as shown in Fig. 5.16. Subfigure a) is relatively similar to the pendant of the ${}^8\text{He}$ runs. Noticeable in b) is the cutoff at $\sim 6^\circ$ opening angle for the particle with the smaller energy loss. In principle, this could be an acceptance effect, where events with large relative angles are not detected by the trigger logic. The statistics in c) is much lower due to a shorter beam time for the ${}^6\text{He}$ runs. Also, events in this gate are not expected. Figure d) has the same shape as its ${}^8\text{He}$ pendant, which again underlines the idea of scattered delta electrons.

Figure 7.7 depicts the distribution of opening angles against the corresponding reaction plane angle. Noticeable is the absence of the 3° band in contrast to the corresponding plot with the ${}^8\text{He}$ beam as in 5.20. The effect is strongly tied to a specific combination of energies of emitted particles and their types.

Since every event is triggered by a particular trigger (see Fig. 2.2), the double energy plots can be redrawn for specific triggers. Figure 7.8 depicts the energy loss of two particles coming from the target plotted against each other for trigger 6, which is the 'Beam x HODOP x HODF24' selection. The statistics are much lower and concentrated around the two excess regions as described in chapter 5.8.

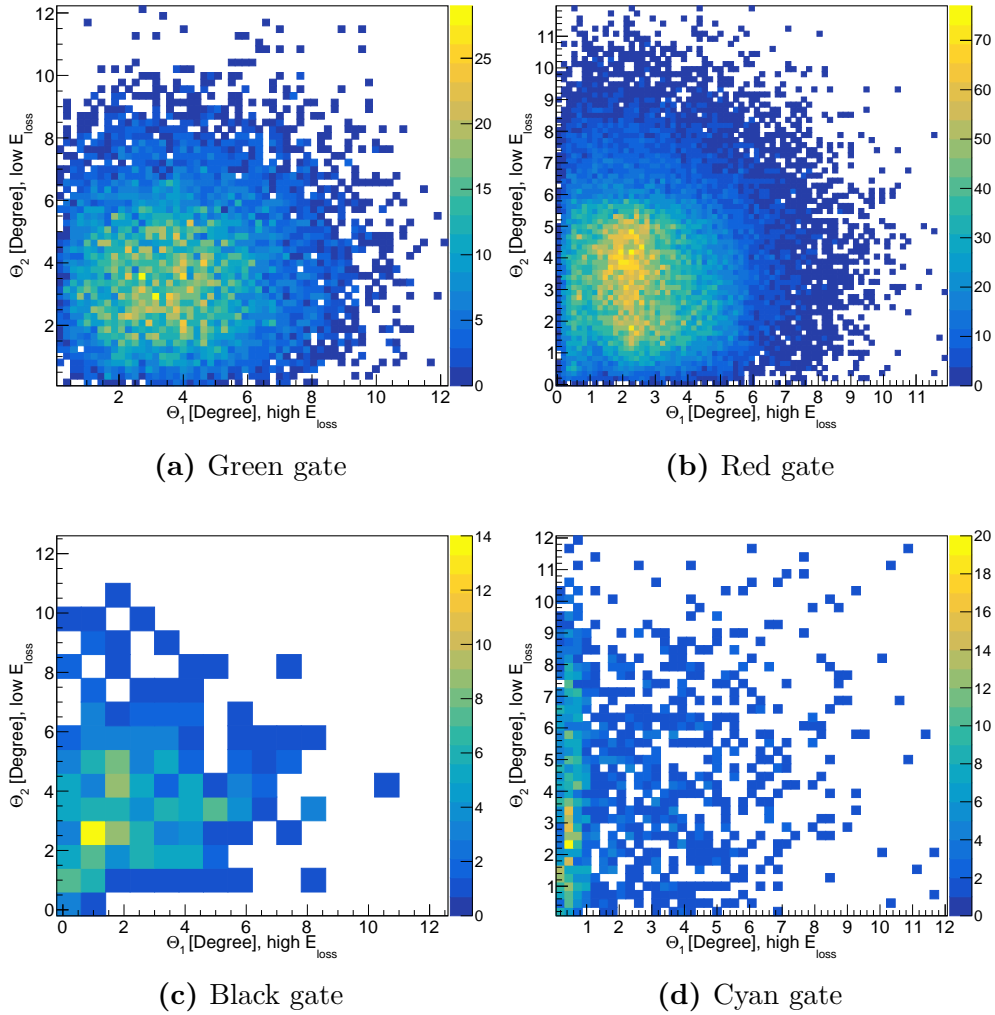


Figure 7.6: Relative opening angles to a hypothetical beam axis plotted against each other for ${}^6\text{He}$ on a full target. Upper left: Both particles have similar energy loss and scatter with the same relative angle to the beam axis. Upper right: The particle with the higher energy loss is in general slower and tends to scatter under larger angles. A cutoff at 6° for the particle with lower energy loss is visible. Lower left: Due to low statistics a final claim cannot be made. Lower right: The particles with the high energy loss scatters with low relative angles to the beam axis while the particles with the low energetic loss scatter under larger angles.

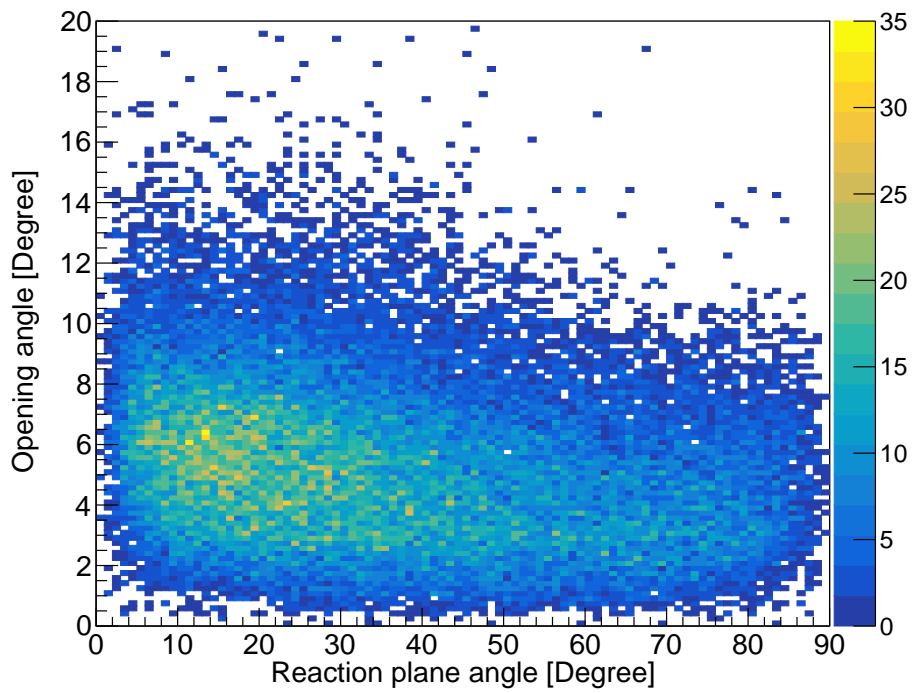


Figure 7.7: Opening angle plotted against the angle of the reaction plane for ${}^6\text{He}$ on target.

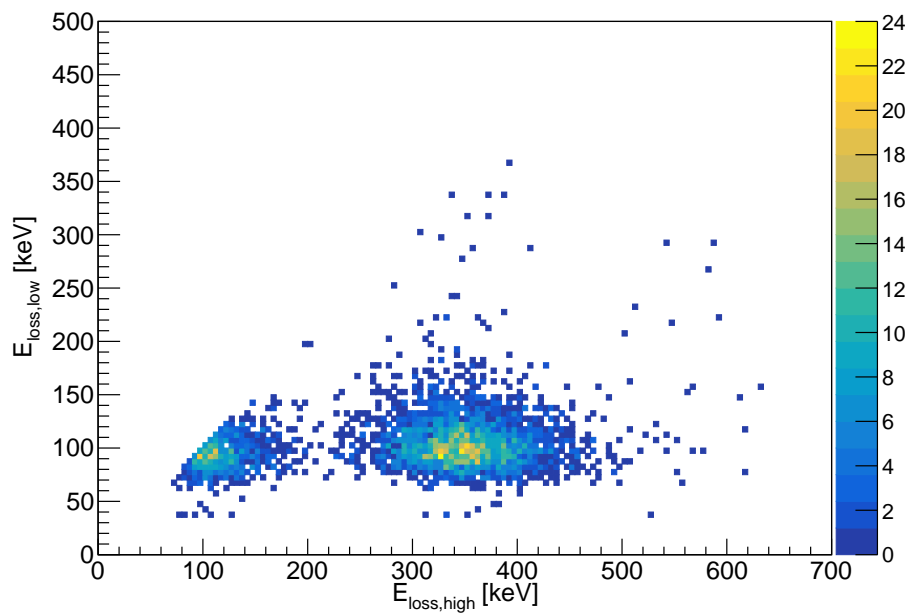


Figure 7.8: Energy loss of particles coming from the target plotted against each other for the trigger 'Beam x HODF24 x HODP'.

7.5 Concept drawings

The detector modules are a composition of an old X-type detector layer with a corresponding copper frame for cooling and a newly designed Y-type detector layer with copper- and cooling frame. A schematic of the is shown in Fig. 7.9.

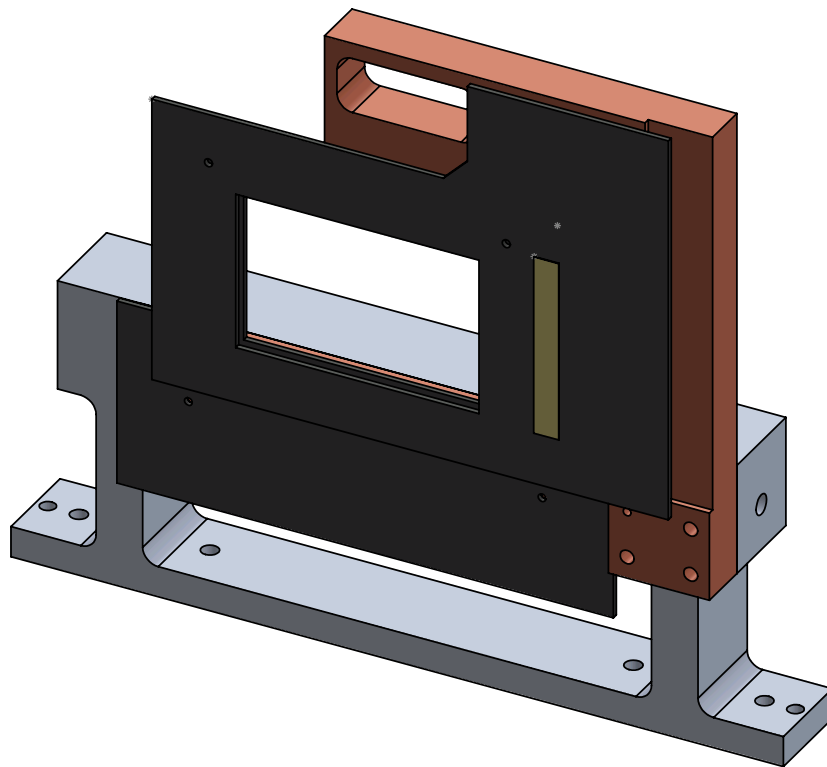


Figure 7.9: Concept drawing of a XY-module. X- and Y-wafer are mounted on copper frames, which in return are placed on a cooling frame.

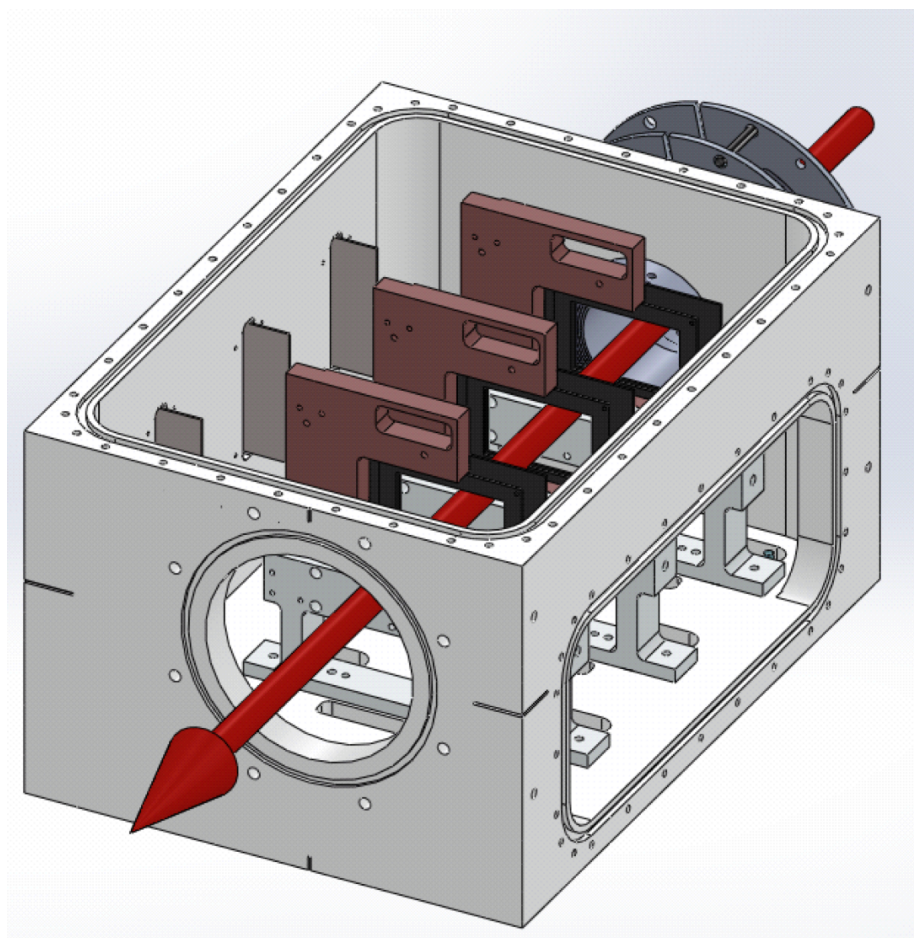


Figure 7.10: Concept drawing of the chamber with detector modules. The beam direction is indicated as a red arrow.

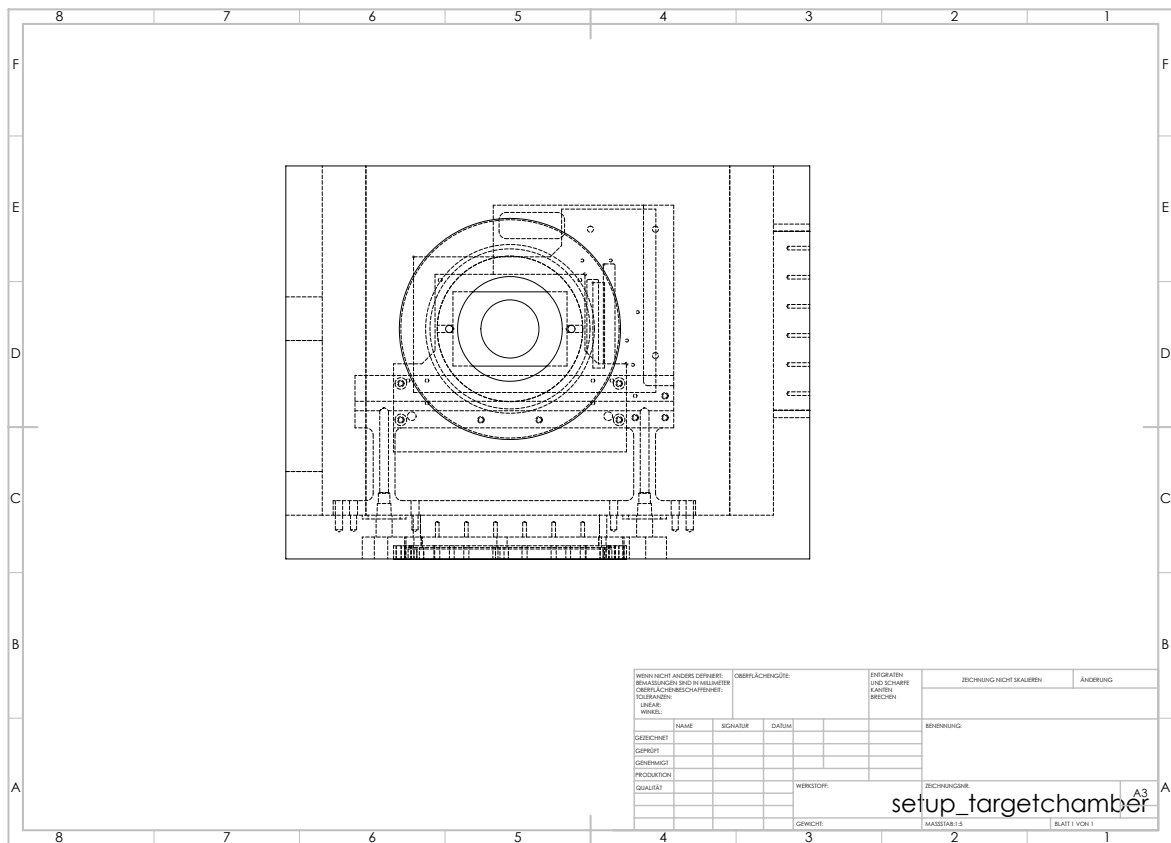


Figure 7.12: Concept drawing of the target chamber from the front with inserted tracking module. The centered circle depicts the position of the target bubble.

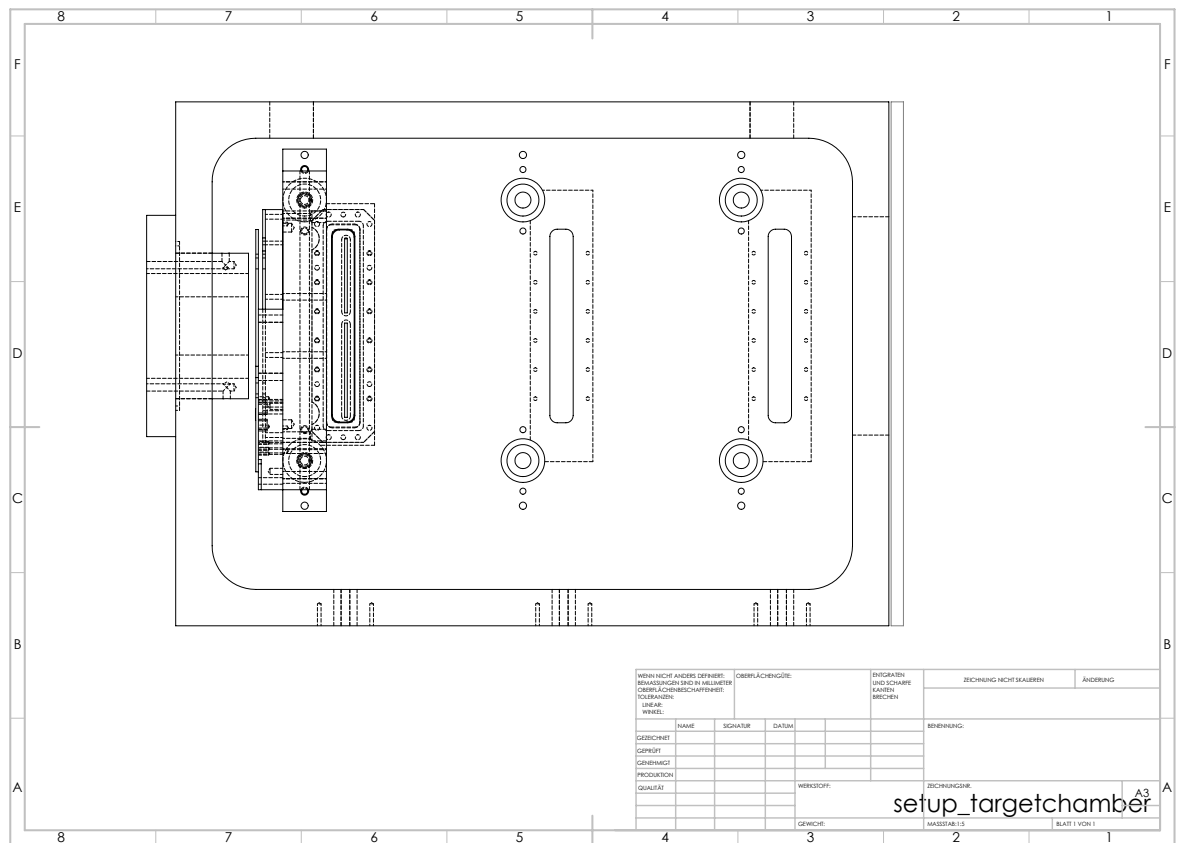


Figure 7.13: Concept drawing of the target chamber with inserted first detector module as seen from above.

Bibliography

- [1] P. B. Demorest, T. Pennucci, S. M. Ransom, M. S. E. Roberts, and J. W. T. Hessels, “A two-solar-mass neutron star measured using Shapiro delay,” *Nature* **467** (10, 2010) 1081 EP –. <http://dx.doi.org/10.1038/nature09466>.
- [2] D. Lonardonì, A. Lovato, S. Gandolfi, and F. Pederiva, “Hyperon puzzle: Hints from quantum monte carlo calculations,” *Phys. Rev. Lett.* **114** (Mar, 2015) 092301. <https://link.aps.org/doi/10.1103/PhysRevLett.114.092301>.
- [3] I. Bombaci, “The Hyperon Puzzle in Neutron Stars,” p. 101002. 2017. [arXiv:1601.05339](https://arxiv.org/abs/1601.05339) [nucl-th].
- [4] K. Hebeler, J. M. Lattimer, C. J. Pethick, and A. Schwenk, “Constraints on neutron star radii based on chiral effective field theory interactions,” *Phys. Rev. Lett.* **105** (Oct, 2010) 161102. <https://link.aps.org/doi/10.1103/PhysRevLett.105.161102>.
- [5] T. Otsuka, T. Suzuki, J. D. Holt, A. Schwenk, and Y. Akaishi, “Three-body forces and the limit of oxygen isotopes,” *Phys. Rev. Lett.* **105** (Jul, 2010) 032501. <https://link.aps.org/doi/10.1103/PhysRevLett.105.032501>.
- [6] B. Alex Brown, “Neutron radii in nuclei and the neutron equation of state,” *Phys. Rev. Lett.* **85** (Dec, 2000) 5296–5299. <https://link.aps.org/doi/10.1103/PhysRevLett.85.5296>.
- [7] R. Lazauskas and J. Carbonell, “Three-neutron resonance trajectories for realistic interaction models,” *Phys. Rev. C* **71** (Apr, 2005) 044004. <https://link.aps.org/doi/10.1103/PhysRevC.71.044004>.
- [8] Y. A. Lashko and G. F. Filippov, “Cluster structure of a low-energy resonance in tetra-neutron,” *Physics of Atomic Nuclei* **71** no. 2, (Feb, 2008) 209–214. <https://doi.org/10.1134/S1063778808020014>.
- [9] F. M. Marqués *et al.*, “Detection of neutron clusters,” *Phys. Rev. C* **65** (Apr, 2002) 044006. <https://link.aps.org/doi/10.1103/PhysRevC.65.044006>.
- [10] F. M. Marques, N. A. Orr, H. A. Falou, G. Normand, and N. M. Clarke, “On the possible detection of 4n events in the breakup of ^{14}Be ,” *ArXiv Nuclear Experiment e-prints* (Apr., 2005) , [nucl-ex/0504009](https://arxiv.org/abs/nuc1-ex/0504009).
- [11] K. Kisamori *et al.*, “Candidate resonant tetra-neutron state populated by the $^4\text{He}(^8\text{He}, ^8\text{Be})$ reaction,” *Phys. Rev. Lett.* **116** (Feb, 2016) 052501. <https://link.aps.org/doi/10.1103/PhysRevLett.116.052501>.

- [12] S. Paschalis and S. Shimoura, “Investigation of the $4n$ system at samurai by measuring p,p α quasifree scattering at large momentum transfer in complete kinematics,”
- [13] T. Kobayashi and the SAMURAI collaboration, “Results from commissioning run in 2012,”
- [14] V. Comparat *Phys. Rev. C* **12**, 251 (1975) .
- [15] “RIBF complex.” <http://www.nishina.riken.jp/RIBF/BigRIPS/concept.html>.
- [16] A. Obertelli *et al.*, “Minos: A vertex tracker coupled to a thick liquid-hydrogen target for in-beam spectroscopy of exotic nuclei,” *Eur. Phys. J. A* **50** no. 1, (2014) 8.
<https://doi.org/10.1140/epja/i2014-14008-y>.
- [17] “The liquid hydrogen target for the MINOS project,”. http://irfu.cea.fr/dacm/en/Phoce/Vie_des_labos/Ast/ast_visu.php?id_ast=3383.
- [18] S. Reichert, “PhD Thesis, TU Munich,”.
- [19] L. Jones, “APV25-S1 User Guide Version 2.2.2001.”
<https://cds.cern.ch/record/1069892/files/cer-002725643.pdf>.
- [20] S. Reichert and M. Sako, “Status of the $(p, 2p)$ silicon tracker for upcoming fission experiments with the samurai spectrometer,” *RIKEN Accel. Prog Rep.* **49** (2016) .
<http://www.nishina.riken.jp/researcher/APR/APR049/pdf/167.pdf>.
- [21] R. Lazauskas and J. Carbonell, “Three-neutron resonance trajectories for realistic interaction models,” *Phys. Rev. C* **71**, 044004 (2005) .

Acknowledgement

I want to thank everyone who supported me during my thesis. This project was a new and highly interesting experience for me and helped me to grow as a physicist and increase my skills in detector design, data analysis and nuclei physics. Especially I want to thank Prof. Laura Fabbietti for her support and the opportunity to be part of this experiment.

I am deeply thankful for the support I received from my supervisors Roman Gernhäuser and Sebastian Reichert and the fruitful discussions we had. They always supported me with knowledge and feedback in all aspects and steered me in the right directions whenever I needed it. I also want to thank Sasano-san for his great support and farsightedness.

I want to thank Michael Böhmer, Vadim Wagner, Fabia Schindler, Dominic Rossi, Stefanos Paschalis, Daniel Körper and Junki Tanaka for their help in realizing this project. A special thanks to the Workshops at TUM Physics Department and at the Lichtwiese in Darmstadt for realizing the tracker. I also want to thank my colleagues Christian Berner, Lukas Werner and Markus Trunk for the good and supportive atmosphere in our office.

I thank my family for their never-ending support, belief and advice.